ARTICLES
https://doi.org/10.1038/s41564-021-00988-8
nature microbiology

Check for updates

Bluetongue virus capsid protein VP5 perforates membranes at low endosomal pH during viral entry

Xian Xia[1,2], Weining Wu[3], Yanxiang Cui[2], Polly Roy[3] and Z. Hong Zhou[1,2]✉

Bluetongue virus (BTV) is a non-enveloped virus and causes substantial morbidity and mortality in ruminants such as sheep. Fashioning a receptor-binding protein (VP2) and a membrane penetration protein (VP5) on the surface, BTV releases its genome-containing core (VP3 and VP7) into the host cell cytosol after perforation of the endosomal membrane. Unlike enveloped ones, the entry mechanisms of non-enveloped viruses into host cells remain poorly understood. Here we applied single-particle cryo-electron microscopy, cryo-electron tomography and structure-guided functional assays to characterize intermediate states of BTV cell entry in endosomes. Four structures of BTV at the resolution range of 3.4–3.9 Å show the different stages of structural rearrangement of capsid proteins on exposure to low pH, including conformational changes of VP5, stepwise detachment of VP2 and a small shift of VP7. In detail, sensing of the low-pH condition by the VP5 anchor domain triggers three major VP5 actions: projecting the hidden dagger domain, converting a surface loop to a protonated β-hairpin that anchors VP5 to the core and stepwise refolding of the unfurling domains into a six-helix stalk. Cryo-electron tomography structures of BTV interacting with liposomes show a length decrease of the VP5 stalk from 19.5 to 15.5 nm after its insertion into the membrane. Our structures, functional assays and structure-guided mutagenesis experiments combined indicate that this stalk, along with dagger domain and the WHXL motif, creates a single pore through the endosomal membrane that enables the viral core to enter the cytosol. Our study unveils the detailed mechanisms of BTV membrane penetration and showcases general methods to study cell entry of other non-enveloped viruses.

Viral entry into host cells is a highly coordinated process that requires crossing the cell membrane without destroying the integrity of the cell. This process is well understood for enveloped viruses such as influenza virus[1], human immunodeficiency virus (HIV)[2] and SARS-CoV-2 (ref. [3]); and is mediated by glycoprotein-induced fusion of the viral envelope with the host cell membrane[4–6]. By contrast, lacking a lipid envelope, non-enveloped viruses are thought to use a variety of mechanisms for cell entry, such as genome injection, target membrane perforation or disruption, none of which is well understood[7,8]. A prominent example of non-enveloped viruses is bluetongue virus (BTV), an endemic livestock pathogen found in both the United Kingdom and the United States and a member of the Reoviridae family[9,10]. Viruses in this family share similar core structures but differ greatly in their outer layers. The BTV core has 120 VP3 monomers in the inner layer and 260 VP7 trimers in the middle layer, which are organized into a $T=2$ and $T=13$ icosahedral lattice, respectively[11,12]. Although lacking a lipid envelope, BTV virion sports two proteins on its exterior surface, the receptor-binding protein VP2 and the membrane penetration protein VP5, which form 60 triskelions and 120 trimers, respectively[13]. In particular, the VP5 trimer is organized around a stem-helix bundle characteristic of fusion proteins of enveloped viruses and contains clusters of histidine residues that sense low-pH environment (6.0–5.0) encountered during the endocytic pathway of cell entry[14]. Conformational change of the VP5 trimer after entering into endosome primes the virus for membrane penetration, similar to that of reovirus[15] and rotavirus[16]. However, in the absence of direct observation of high-resolution structures in low-pH conditions and membrane-attachment intermediates, the chemical details of low-pH-triggered cell entry by BTV, or any other non-enveloped viruses, remain undefined and, consequently, their exact mechanisms poorly understood.

A major challenge to understanding the mechanism of BTV entry into host cells from endosome is to capture and visualize intermediate states of the virus interacting with endosomal membrane. Here we investigated structural rearrangements of BTV by changing the pH on cryo-electron microscopy (cryo-EM) grids and determined the structures of intermediate states by combining the methods of single particles cryo-EM and cryo-electron tomography (cryo-ET). By testing functional predictions with structure-guided mutagenesis, we recapitulated the detailed mechanism of low-pH-triggered membrane penetration by BTV, from low-pH sensing, stepwise structural rearrangements, membrane insertion, pore formation and viral passage through the pore.

Results

Overall structures of BTV at low pH. To obtain structures of BTV at low pH and investigate the mechanism of membrane penetration, we recorded cryo-EM images of BTV together with liposomes at acidic pH (5.5) and carried out single-particle analysis. We used a stepwise symmetry-guided subparticle reconstruction and classification workflow to sort out and resolve different functional states of both the receptor-binding protein VP2 and membrane penetration protein VP5 at near-atomic resolution (Fig. 1a–c, Extended Data Figs. 1, 2g,h and 3 and Supplementary Table 1). The BTV structure at low pH is drastically different from that at high pH. Two-dimensional (2D) images and slices of three-dimensional (3D) reconstruction clearly show different features of outer-layer proteins of BTV in different conditions (Extended Data Fig. 2a–f). Previous icosahedral cryo-EM structures of BTV at pH 8.8 have shown that

[1]Department of Microbiology, Immunology & Molecular Genetics, University of California, Los Angeles, Los Angeles, CA, USA. [2]California NanoSystems Institute, University of California, Los Angeles, Los Angeles, CA, USA. [3]Department of Pathogen Molecular Biology, London School of Hygiene and Tropical Medicine, London, UK. ✉e-mail: Hong.Zhou@UCLA.edu

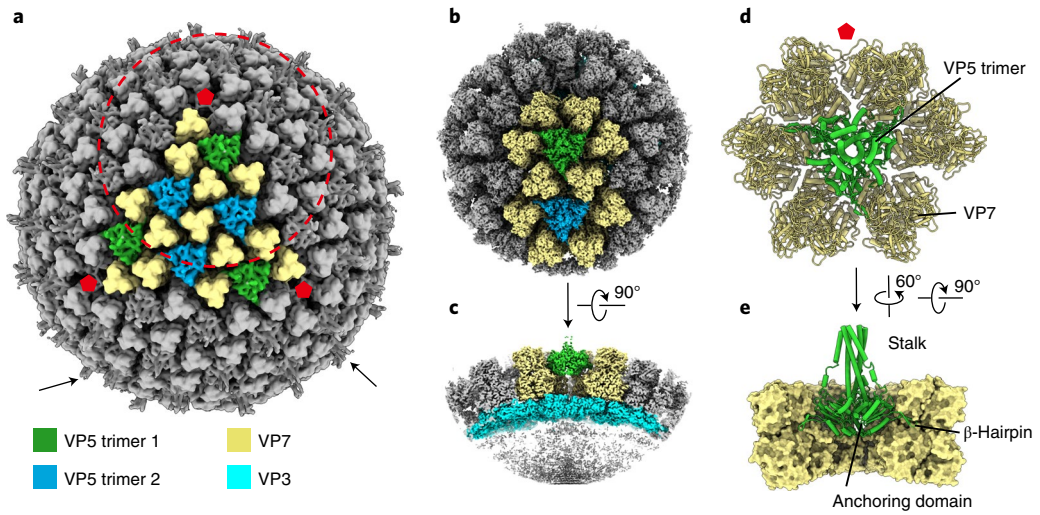

Fig. 1 | Cryo-EM reconstruction of BTV at low pH. a, Icosahedral reconstruction of BTV at low pH. Proteins in one facet of the icosahedron are coloured. The red pentagons indicate the three five-fold vertices of the facet. Dashed circle demarks the area for subparticle reconstruction. Black arrows point to two protruding VP5 stalks. **b**, One of the four subparticle reconstructions, representing the low-pH state, with two VP5 trimers and their surrounding VP7 trimers coloured as in **a**. **c**, Side view of the central slab of **b** showing the relative locations of VP5 trimer 1 (green), VP7 trimers (yellow) and VP3 layer (cyan). **d**, Atomic model of VP5 trimer 1 and the surrounding VP7 trimers at low-pH state. Model is shown in cartoon with helix shown as cylinder. **e**, Side view of the atomic model in **d** without the two front VP7 trimers. VP5 is shown as cartoon and VP7 as surface.

each virion contains 120 globular-shaped VP5 trimers and that each VP5 monomer consists of three domains: dagger, unfurling and anchoring[14]. At low pH, the VP5 trimer transforms into an elongated shape with a stalk protruding from a triangular base (Fig. 1d,e). A surface loop (amino acid A409–A421) from the anchoring domain of each VP5 monomer transforms into a β-hairpin and inserts into a crevice formed between two adjacent VP7 trimers to anchor VP5 to the BTV core (Fig. 1e). Within the asymmetric unit, the structures of VP5 trimer 1 and VP5 trimer 2 are nearly identical, except for slight differences in the anchoring β-hairpins and the positions of their surrounding VP7 trimers (Extended Data Fig. 4a,b). Hence, we will focus only on VP5 trimer 1 and simply refer to it as VP5 trimer below.

Capturing multiple intermediate states. We captured four states of structural transition of BTV on exposure to low pH. These four structures share common features for all domains of VP7 and the anchoring domain of VP5 but differ in the stalk of VP5 trimer and the presence/absence of VP2. Among these, the one with VP2 lost on both sides represents the final low-pH state (Fig. 2a). The other three structures, with VP2 retained on both sides, only on the 'left' side, or the 'right' side, are designated as intermediate states 1 (IMS1), 2 (IMS2) or 3 (IMS3), respectively (Fig. 2a). Compared to their structures on BTV at high-pH state, the three states of the VP5 trimer captured at low pH have drastic conformational changes, while the overall structure of the VP2 trimer does not change. The structures of the VP5 trimer in IMS1 and IMS2 are the same, with the unfurling domain of only one of the three VP5 subunits continuing to interact with the anchoring domain of the same subunit. In IMS3 and the low-pH state, by contrast, the unfurling domains in all three subunits of the VP5 trimer detach and form a stalk (Fig. 2b). The stalk is a coiled-coil bundle of six helices, resembling that of the postfusion state of class I membrane fusion proteins[1,3,17]. Because the sample was flash-frozen on grids after incubation at low pH for 30 s, these stepwise changes of the stalk should have occurred within this time frame. In line with our observations, the smFRET measure of time frame for the low-pH-triggered conformational change of influenza virus haemagglutinin indicated that pH-dependent structure changes of viral fusion/penetration proteins occurred in the time frame of several seconds[18].

VP5 transforms, VP7 moves, VP2 detaches. Careful comparisons between the above-described BTV structure of low-pH state with that of high-pH state indicate that global structural rearrangements involve three capsid proteins: VP2, VP5 and VP7. At high pH, VP5 interacts with VP7 extensively, with a total buried surface area of ~8,000 Å^2 for each VP5 trimer. This interaction involves all three domains—dagger, unfurling and anchoring—of VP5 (Extended Data Fig. 5a). After being exposed to low pH, these dagger domains are no longer visible, indicating that they have become flexible. The three stem helices of VP5 trimer in the low-pH state form a continuous helix bundle together with a portion of the unfurling domain. This bundle is longer and more compact than that of the high-pH state (Fig. 2d and Supplementary Video 1). The anchoring domain of VP5 rotates about 20° towards the virus. Among the three domains of VP5 interacting with VP7 at high pH, only the anchoring domain interacts with VP7 at low pH; moreover, instead of being hidden within VP5 itself at high pH, the β-hairpin now inserts into the interface of two neighbouring VP7 trimers (Extended Data Fig. 5b). As a result of these changed interactions, the buried surface of VP5 trimer shrinks dramatically to 3,430 Å^2, making it easier for the VP5 trimer to detach from BTV core.

Interestingly, the changes in the dagger and anchoring domains of VP5 but not the unfurling domain, are the same in all of the intermediate and low-pH states, indicating that low-pH-triggered conformational changes begin at these two domains. Although both of the VP2 trimers are retained in the IMS1, VP5 adopts the low-pH conformation except for the unfurling domain of one VP5 monomer in the trimer, which remains in the original position. These observations suggest that interactions at the pH sensor are the key factor to stabilize the high-pH conformation of VP5. It is conceivable that low pH triggers the changes first at the pH sensor in the anchoring domain, leading to the relatively 'fast' freeing of the surface loop (to become the anchoring β-hairpin) and the releasing of the dagger and the eventual, 'slow' unfurling of the unfurling domain. This movement occurs even when some VP2

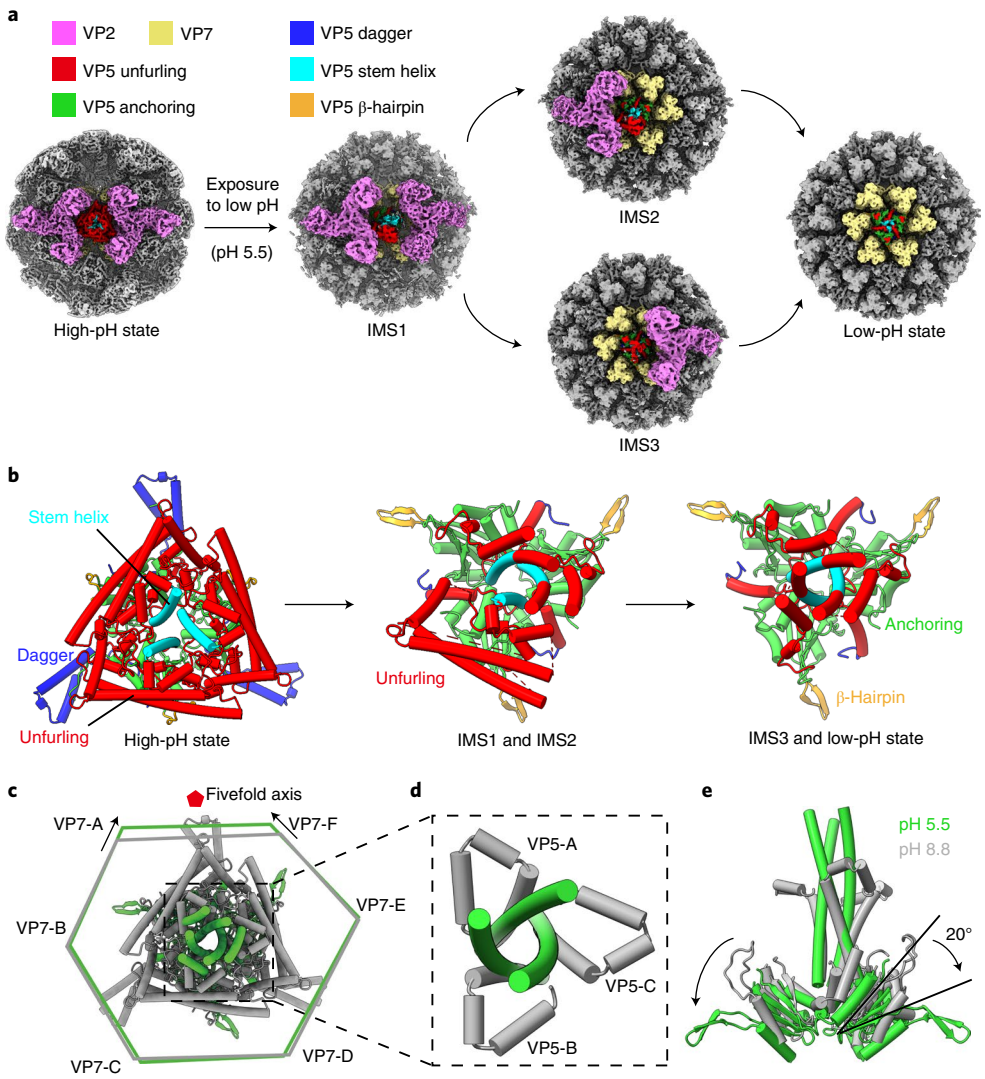

Fig. 2 | Stepwise structural rearrangements of BTV on exposure to low pH. a,**b**, Low-pass filtered (4 Å) subparticle reconstructions (**a**) and atomic models of the VP5 trimer (**b**) of three intermediate states (IMS1–3) and the low-pH state of BTV on exposure to low pH, compared with the structure of high-pH state[14]. **c**–**e**, Subtle movement of VP7 trimer and drastic refolding of VP5 trimer on exposing BTV to low pH. The structures of BTV are aligned by matching their VP3 layers (not shown for clarity), which are identical at the two pH conditions. In the superposition, the structures of high pH and low pH are shown in grey and green, respectively; the VP5 trimer is represented by cylinders (for α helices) and ribbons (for β sheets), whereas the six surrounding VP7 trimers by a hexagon (each vertex of the hexagon is the centre of the three G199 residues in each VP7 trimer). In the top view (**c**), the six VP7 trimers are named VP7-A to VP7-F anticlockwise starting from the five-fold axis. Two of the six VP7 trimers (VP7-A and VP7-F) experienced subtle movement (arrows) towards the fivefold axis and the rest did not move. By contrast, the VP5 trimer exhibited two drastic conformational changes: first, the helix structures (amino acid P90 to N135) of all three subunits (VP5-A through VP5-C) of the VP5 trimer refolded into the stalk (**d**); second, as indicated by the arrows in the side view (**e**), the anchoring domain rotate 20° towards the VP3 layer.

trimers remain on the capsid (Fig. 2a), indicating that the movement is not related to the status of VP2. The conformational changes of VP5 are accompanied by movement of two VP7 trimers (VP7-A and VP7-F) towards the fivefold axis approximately 6 Å (Fig. 2c and Supplementary Video 1). These changes in VP5 and VP7 weakened the interactions between VP2 and VP5, leading to the stepwise detachment of VP2 (Fig. 2a).

Atomic details of the VP5 transformation. Among the three capsid proteins undergoing conformational changes at low pH, the structures of VP5 are dramatically different between the two pH conditions (Fig. 3a,b). In a VP5 trimer, the three protomers are almost identical except for a slight difference on the β-hairpins (Extended Data Fig. 4c,d). Among the domains within a protomer, only the anchoring domain between the two pH conditions can be superposed (Fig. 3b); the other two domains—dagger and unfurling—both undergo drastic conformational changes. First, the dagger domain at high pH was stabilized by β7 and β9 at N and C termini, respectively. However, β2, originally sandwiched by β3 and β9, refolded into an α-helix atop the anchoring domain at low pH (Fig. 3c). The dagger domain at low pH is largely flexible, potentially being able to interact with the membrane. Second, the unfurling domain and the surface loop in the anchoring domain are stacked together by a clustering of unprotonated histidine residues—the pH sensor—at high pH (Extended Data Fig. 6a). Protonation of these histidine residues at low pH resulted in dissociation of both the unfurling domain and the surface loop from the anchoring domain (Extended Data Fig. 6b). The three freed unfurling domains then

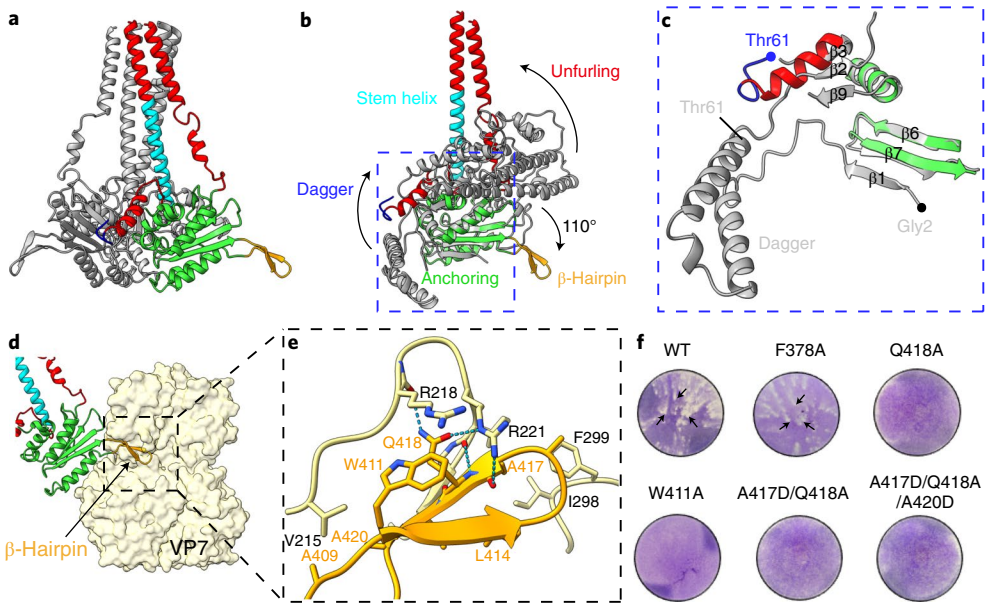

Fig. 3 | Conformational changes in VP5 on exposure to low pH. a, Structure of VP5 trimer in low-pH state with subunit VP5-B coloured as in Fig. 2b and the subunits VP5-A and VP5-C in grey. **b**, Superposition of VP5-B at low pH (colour) with VP5 at high pH (grey). Arrows indicate directions of domain movements on low-pH exposure. **c**, Structure of the dagger domain in the boxed region of **b**, highlighting refolding of a β strand and its connecting loop into an α helix in the N termini of VP5 on low-pH exposure. **d**, Interactions between the anchoring β-hairpin and VP7 trimer (yellow surface). **e**, Enlarged view of the boxed region in **d** with interacting side chains and hydrogen bonds between the VP5 β-hairpin and VP7 shown as sticks and cyan dashed lines, respectively. **f**, Plaque formation at 72 h posttransfection by reverse genetics with BTV genome carrying indicated single, double and triple VP5 mutations in the β-hairpin, compared with that by the wild type (WT) and positive control (VP5 F378A). Plaques are indicated with black arrows.

bundled into an outward-protruding stalk (Fig. 3a and Extended Data Fig. 6c).

The loop from A409 to A421 rotates 110° and transforms into a β-hairpin (Fig. 3b and Extended Data Fig. 6c). The three newly formed β-hairpins of a VP5 trimer each insert into a groove on the waist of an underlying VP7 trimer (Fig. 3d), anchoring the VP5 trimer to the BTV core. Aside from the main chain interactions between β strands of VP5 and VP7, the β-hairpin is stabilized by hydrogen bonds between the side chains of Gln418 of VP5 and Arg218 and Arg221 of VP7 and by hydrophobic interactions between VP5 and VP7 around residues A416 and A420 on VP5, as well as cation-π interaction between the side chain of VP7 R218 and the indole ring of VP5 W411 (Fig. 3e). These interactions comprise a total of ~1,650 Å^2 of buried area between a VP5 trimer and the surrounding VP7 trimers. Although this buried area is about half of the 3,430 Å^2 buried surface between a VP5 trimer and VP7, the interactions in this area are the main contributing elements maintaining contact of VP5 to the BTV core, as there is no specific residue–residue interaction elsewhere. Compared with the BTV structure at high pH, the VP5 residues involved in VP7 interaction at low pH have no contacts with VP7 at high pH. To test the significance of these interactions on virus replication, we carried out a series of structure-guided mutagenesis studies (Fig. 3f). Among them, single (Q418A, W411A), double (A417D/Q418A) or triple (A417D/Q418A/A420D) mutations were introduced to the VP5-encoding gene in the BTV genome and each was subjected to virus recovery assay using reverse genetics system[19,20]. These mutations did not disrupt the VP5 protein expression (Extended Data Fig. 7a) and its interaction with VP7 at high pH (Extended Data Fig. 7b); however, none yielded viable viruses on the basis of virus recovery assays (Fig. 3f). The controls, transfections with the wild type and a mutation (F378A) adjacent to the anchoring β-hairpin but not involved in VP7 interaction both showed plaque formation with similar morphology, indicating virus replication was not perturbed (Fig. 3f). These mutagenesis studies on VP5 indicate that, although not important for VP5 folding and BTV assembly at high pH, residues at the β-hairpin involved in VP7 interaction at low pH are essential for BTV replication at the step of cell entry through endosome. In addition, corresponding residues in VP7 were also mutated, including R218A, I298D and V215D. Although these mutations had no detrimental effect on VP7 expression (Extended Data Fig. 7a), no virus was recovered when transfected with these mutated genomes (Extended Data Fig. 7c). Overall, VP5 undergoes dramatic conformational changes in all three domains and anchors to VP7 through the newly formed β-hairpin at low pH.

VP5 inserts its stalk tip into membrane. Next, we explored how BTV interacted with membrane after exposure to low pH with cryo-ET and subtomogram averaging. Specifically, we applied purified BTV virions to grids and washed them with liposome-containing solutions at neutral pH (7.5), low pH (5.5) and pH shift (that is, at low pH first and then washed with buffer at neutral pH to mimic the condition of virus entering into cell cytosol) conditions. Computational slices from the 3D tomograms clearly resolved characteristic features of viruses and liposomes (Fig. 4a and Extended Data Fig. 8a,b). At neutral pH, most particles are intact virions, as are those at high pH. As expected, due to absence of receptors on liposomes, no viral particles have interactions with the membrane at neutral pH (Extended Data Fig. 8a). At low pH, BTV undergoes structural rearrangements and forms an intermediate with long stalk protruding out from the viral core (Fig. 4a-c and Supplementary Video 2), consistent with high-resolution structures from single-particle cryo-EM reconstruction described above (Fig. 1a). Change of pH from 5.5 back to 7.5 did not reverse these structural rearrangements (Extended Data Fig. 8b and Supplementary Video 3). The proportion of intact virions decreases from 85% at neutral pH to 15% at low pH and even further when changed back to neutral pH (Extended Data Fig. 8c). Concomitantly, the propor-

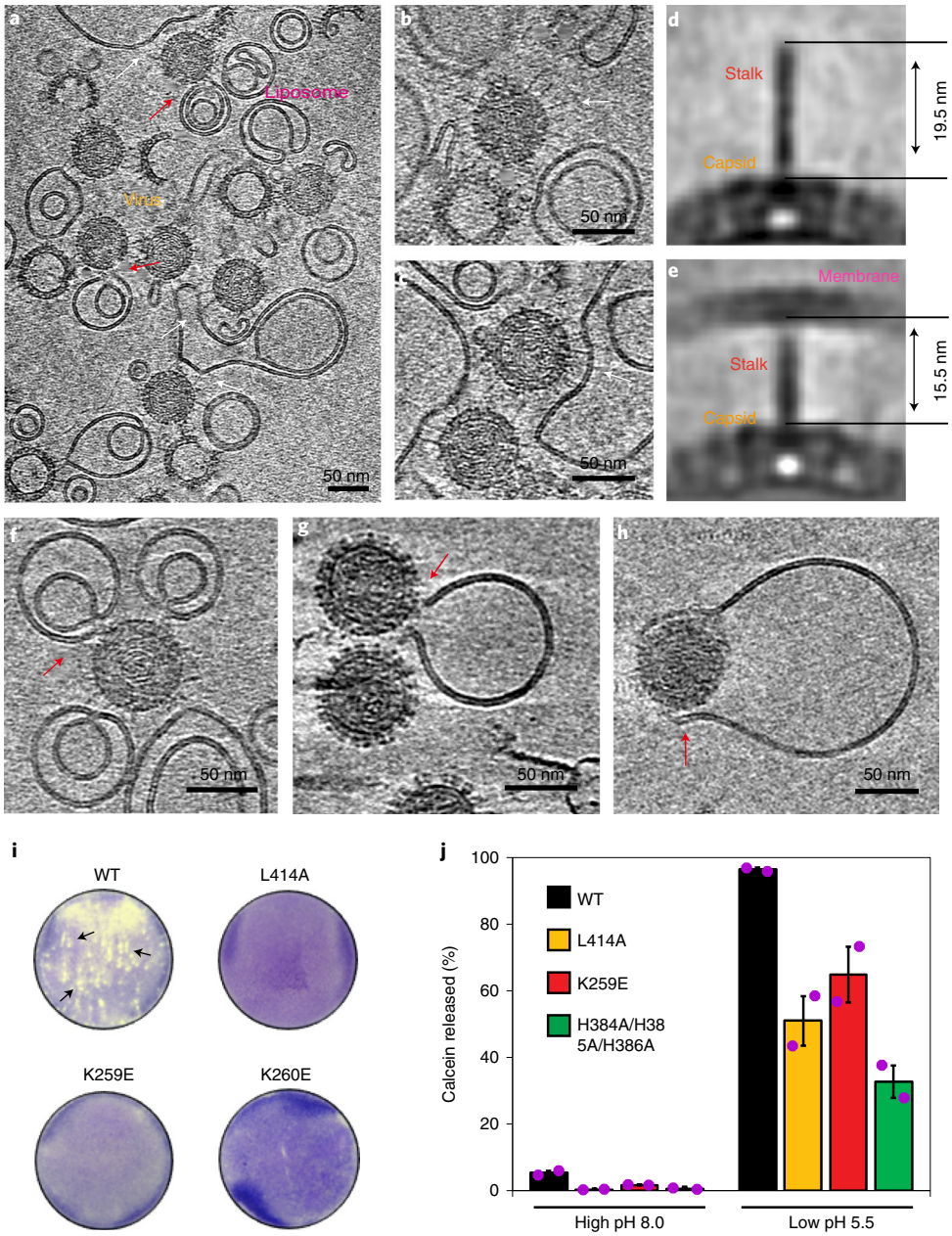

Fig. 4 | Interaction of BTV with liposomal membrane. a, A slice from a cryo-ET reconstruction of BTV particles incubated with vesicles in low-pH condition. White arrows point to interacting regions of VP5 stalk with membrane, whereas red arrows indicate pores on the liposomal membrane generated by BTV. The data shown are representative results of two independent experiments. **b**,**c**, Slices of cryo-ET reconstruction containing viral particles with membrane-free stalks (**b**) and membrane-wrapped stalks (**c**) in low-pH condition. **d**,**e**, Central slices of a subtomogram average for membrane-free stalk (**d**) and membrane-wrapped stalk (**e**) in low-pH condition. **f**, A slice of a representative tomogram showing a pore (arrow) generated on liposomal membrane by BTV at low pH. **g**,**h**, Slices of cryo-ET reconstruction of the pH-shift condition showing membrane pore expansion and accommodated virus passage (arrow). **i**, Plaque formation by reverse genetics from three VP5 single mutations within the penetration elements, compared with that by the wild type (WT). Plaques are indicated by black arrows. **j**, Comparison of membrane permeability at high and low pH by wild type (WT) VP5 and its various mutants, as measured by calcein release from liposomes with compositions mimicking that of late endosomal membrane. The data represent mean values (histograms) ± s.d. (error bars; $n = 2$ biological independent experiments).

tions of intermediate and core particles increase, respectively, from 0 and 15% at high pH to 57 and 28% at low pH and further to 61 and 38% when pH was changed back to 7.5 (Extended Data Fig. 8c). These results indicate that low pH alone can induce structural rearrangements of BTV efficiently and this process is irreversible.

Further subtomogram averaging analysis reveals interaction details between the low-pH conformation of VP5 and the vesicle membranes. At low pH, VP5 stalks interact with vesicle membranes, introducing either curved or distorted surface areas on liposomes (Fig. 4a). Many VP5 stalks at low pH appear to interact with membranes (Fig. 4a), although some are also free from membrane interactions (membrane-free stalk) (Fig. 4b). In the former case, the viral particle can be wrapped by an invaginating membrane area, giving rise to many membrane-wrapped stalks (Fig. 4c). The lengths of membrane-free and membrane-wrapped stalks are about 19.6 and 15.7 nm, respectively (Extended Data

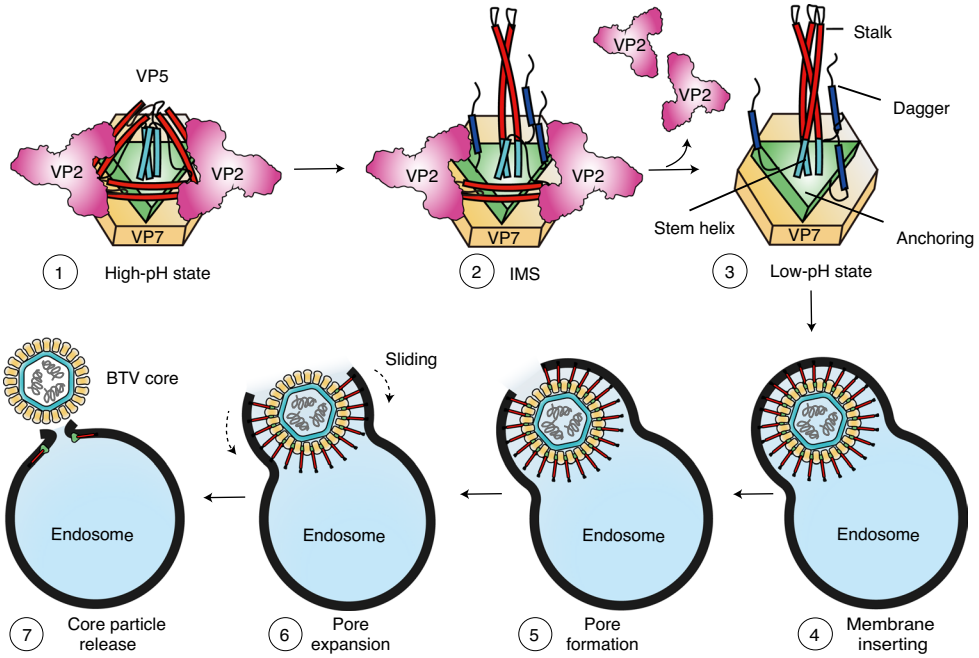

Fig. 5 | Mechanistic model of BTV membrane penetration. Different domains of VP5 are coloured with dagger domain in blue, stem helices in cyan, unfurling domain in red and anchoring domain in green. Arrows show the process of structure transition and membrane penetration. The upper row shows conformational changes of a VP5 trimer and its neighbouring VP2 and VP7 on exposure to the low-pH condition. The lower row illustrates the stepwise structural rearrangements of BTV inside the late endosome, leading to the formation of a pore, enlargement of the pore and eventually the passage of the BTV core through the pore.

Fig. 8d,e). Subtomogram averages from about 100 subvolumes of such stalks reveal that the VP5 trimer sits atop six surrounding VP7 trimers (Extended Data Fig. 9a–d), as seen in the high-resolution single-particle cryo-EM reconstructions (Fig. 1b,c). The lengths of the stalks were further confirmed by subtomogram averaging, decreased from 19.5 to 15.5 nm after interacting with the membrane (Fig. 4d,e). The change of stalk lengths after membrane interaction indicates that the tip portion of the stalk (about 4 nm in length) has possibly inserted into the liposomal membrane (Extended Data Fig. 9e). At the current resolution, we cannot exclude the possibility that the tip portion lies flat on the membrane with key residues interacting with membrane at the level of the lipid head groups.

BTV in the act of membrane penetration. Next, we asked whether BTV at low pH can penetrate through the membrane. After interacting with the membrane at low pH, viral particles approached the liposomal membrane and created a single pore at the site of the stalk–membrane interaction (Fig. 4a,f and Extended Data Fig. 8g,h). This creation of a single pore, rather than large perforated membrane areas, is consistent with prior biochemical experiments showing that, at low pH, reovirus could enable release of fluorescent molecules of 10 kDa—but not those of 40 kDa—from vesicles[21]. In the tomograms of the pH-shift experiment, the pore at the site of attachment on the liposomes appeared to be further expanded, allowing passage of the full viral particle (Fig. 4g,h and Extended Data Fig. 8b,i,j).

What elements of VP5 participate in this highly dynamic process? Subtomogram averaging shows that the tip portion of the stalk inserts into the membrane (Extended Data Fig. 9). Our hypothetic model of the full-length VP5 maps the membrane-binding site to the region of basic and hydrophobic sequence (R250–K260) at the stalk tip (Extended Data Fig. 9e,f). This sequence bears similarity to the phosphoinositide (PI)-binding motif (K/R-(Xn = 3–7)-KXKK) (refs. [22,23]) and has the potential to bind negatively charged lipids. Interestingly, the negatively charged lipid lysobisphosphatidic acid (LBPA) was found to be enriched in the late endosomal membrane[24,25] and important for BTV membrane penetration[26]. To evaluate the functions of this membrane penetration element and the previously suggested WHXL motif[14,27], we introduced two mutations in the stalk tip (K259E, K260E) and one mutation (L414A) in the WHXL motif[14,27] in the BTV genome and performed a virus recovery assay by reverse genetics. As expected, contrary to the situation with the wild type, transfection with mutant genomes all failed to generate infectious virus (Fig. 4i), despite successful synthesis of the mutant VP5 protein (Extended Data Fig. 7d). The two VP5 mutant proteins (L414A and K259E) were purified and their membrane penetration activities were further investigated with a liposome calcein release assay. As shown by gel-filtration and negative staining electron microscopy, purified VP5 is a trimer and has conformational change after low-pH treatment (Extended Data Fig. 7e,f). Results from calcein release assay show that the high activity of VP5 at low pH was reduced by ~47% and ~33% for mutants L414A and K259E, respectively (Fig. 4j). The negative control assay with VP5 triple mutant (H384A/H385A/H386A) in the pH sensor showed a 66% reduction of membrane penetration activity. In addition, our result presented in the previous section (Fig. 3c) showing that low pH freed the dagger domain of VP5 also explains the observed membrane penetration activity of the dagger domain[26,28]. Taken together, the structural and biochemical data indicate that three VP5 elements—the tip portion of the stalk (R250–K260), the WHXL motif and the dagger domain—must work together for the virus to penetrate the endosomal membrane and release its core into the host cell cytosol.

Discussion

Our data captured multiple intermediate states of BTV on exposure to low pH, demonstrating stepwise structural rearrangements of BTV interacting with liposomal membrane, mimicking that in

the host cell. We visualized BTV in the act of membrane penetration and identified the tip part of the low-pH-triggered VP5 stalk as an element important for membrane penetration, in addition to the dagger domain and the WHXL motif. Together, our structural and biochemical data unveil the molecular mechanism for membrane penetration and put forward a model for cell entry by BTV, as illustrated in Fig. 5. Briefly, attachment of VP2 to receptors on the host cell membrane enables BTV entry into endosomes through endocytosis. Protonation of the pH sensor of VP5 in the late endosome disrupts the meta-stable neutral pH conformation and unfurls the unfurling domain, leading to the lower energy, low-pH form of the VP5 trimer, which has a long stalk protruding outward from the BTV core (Fig. 5, stages 1 to 3). Exposure to the low-pH environment in the late endosome also triggers the stepwise detachment of VP2 (Fig. 5, stages 2 and 3). The released energy in this process may facilitate insertion of the stalk tip into the endosomal membrane (Fig. 5, stage 4); consequently, the dagger domain and the WHXL motif would now be brought into the vicinity of the membrane for membrane-disruptive interactions, leading to the formation of a small pore on the endosomal membrane (Fig. 5, stage 5). Participation by VP5 trimers near this pore and detachment of the VP5 already interacting with membrane[29] gradually increase the size of the pore to allow the passage of the viral core without disrupting the entire endosomal membrane (Fig. 5, stage 6). Finally, passage through the enlarged pore releases the viral core into the host cytosol (Fig. 5, stage 7), where availability of substrates would trigger endogenous RNA transcription and assembly of progeny viral particles[30,31]. Herrmann et al.[32] reported that rotavirus attaches to its host cell through its outer-layer protein VP4, which—following cleavage—rearranges to enable perforation of cell membrane. Although the structural rearrangements on the capsid proteins are different, BTV and rotavirus are similar in that the penetration proteins protrude from the core and interact with the target membrane, suggesting that our model of membrane penetration by BTV is applicable to other non-enveloped viruses.

In summary, we have captured intermediate states of structure transition and membrane penetration of BTV at low pH for the first time and put forward a model for endosomal cell-entry mechanism of BTV, a representative of large, non-enveloped RNA viruses. Testing of functional consequences of mutating residues involved in the key interactions further supports this model. Our study opens the door for understanding cell entry by other non-enveloped viruses and ultimately for designing drugs to block this essential infection step.

Methods

Virus purification. Cell culture and purification of intact BTV virion were similar to procedures described before[13] with some modifications. Briefly, baby hamster kidney cells (BKH-21, ATCC-CCL10) were infected with BTV-1 at 90% confluence and harvested at about 70 h postinfection. Only the cells were collected for virus purification. The cells were lysed in 100 mM Tris-HCl, pH 8.8, 50 mM NaCl, 0.1% v/v NP40 and protease inhibitor at 4 °C for 15 min. The resulting lysate was then centrifuged at 2,000*g* for 10 min to pellet nuclei. The supernatant which contained intact virions released from the cells was loaded onto a double cushion with 4 ml of 66% (w/w) sucrose on the bottom and 10 ml of 50% (w/v) sucrose on the top. The sample was centrifuged at 100,000*g* using an SW 28 rotor for 1 h at 4 °C. The band at the interface of the two sucrose cushions was collected and diluted ten times in 20 mM Tris-HCl (pH 8.8). The sample was then incubated on ice for 10 min after adding *N*-lauroylsarcosine sodium salt (Sigma Aldrich) to a final concentration of 0.1% to reduce aggregation of the sample. The sample was clarified by centrifugation at 16,000*g* for 10 min and then the supernatant was pelleted through 1 ml of 30% (w/v) sucrose cushion at 80,000*g* for 1 h at 4 °C in SW 41 Ti rotor. Finally, the supernatant was carefully removed and the pellet was resuspended in 20 µl of 20 mM Tris-HCl at pH 8.8. For BTV core particles, band from the interface of double cushion was further purified in self-forming CsCl gradients as described before[33].

Liposome preparation for cryo-EM and cryo-ET. Liposomes for cryo-EM were prepared[34] from 1,2-dioleoyl-sn-glycero-3-phosphocholine, 1,2-dioleoyl-sn-glycero-3-phosphoethanolamine, cholesterol (ovine) and LBPA in a molar ratio of 50:20:15:15. All lipids were purchased from Avanti polar lipids and dissolved in chloroform at a concentration of 25 mg ml^{-1}. The four lipids were then mixed in a glass vial using glass syringes (Hamilton). The chloroform was evaporated under nitrogen gas and the remaining traces of solvent were removed by placing the glass vial in a vacuum desiccator for 3 h. Next, the dried lipids were hydrated in liposome buffer (10 mM HEPES pH 7.5, 50 mM Na citrate, 100 mM NaCl) at 20 mg ml^{-1}. The mixture was freeze-thawed five times in liquid nitrogen and then extruded 21 times through a 0.2-µm polycarbonate membrane filter by using a Mini Extruder (Avanti Polar Lipids). The resulting liposomes were stored at 4 °C and used freshly.

Cryo-EM sample preparation and image collection. To prepare cryo-EM grids for single-particle analysis, liposomes were titrated to pH 5.5 with citrate buffer. A total of 2 µl of purified BTV virion was applied to a glow discharged, thin continuous carbon film coated Lacey grid (Ted Pella). After incubation for 1 min, the sample on the grid was blotted manually with filter paper and 2.5 µl of acidified liposomes were added to the grid. After incubation for another 30 s, the grid was blotted for 20 s at 8 °C with 15 blot force and 100% humidity and plunge-frozen in liquid ethane by using a Vitrobot Mark IV (Thermo Fisher Scientific). For grids of cryo-ET at low pH, grids were prepared in the same way except that liposomes were mixed with 10-nm gold beads before being applied to the grid. For grids of cryo-ET at neutral pH, liposomes without acidification were used. For grids in the pH-shift condition, 2 µl of BTV virion was applied to a grid and incubated for 1 min. Next, the grid was manually blotted and washed with 2.5 µl of acidified liposomes and incubated for 30 s. The grid was then manually blotted and 2.5 µl of liposome buffer with gold beads was added to the grid and incubated for another 30 s before blotting by Vitrobot Mark IV in the same condition as above. Grids of BTV virion and core were prepared similarly without liposomes.

Those grids were loaded to a Titan Krios electron microscope (Thermo Fisher Scientific) equipped with a Gatan imaging filter (GIF) Quantum LS and a Gatan K2 Summit direct electron detector. The microscope was operated at 300 kV at super-resolution mode. Videos were recorded as dose-fractionated frames (0.2 s per frame) with SerialEM[35]. For single-particle reconstruction, videos were recorded at a nominal magnification of ×105,000, corresponding to a calibrated pixel size of 0.68 Å on the specimen level in super-resolution mode. Defocus was set to −1.8 to −2.6 µm. The total exposure time for each video was set to 8 s, fractionated equally into 40 frames, leading to a total dosage of 40–50 electrons per Å^2 on the specimen.

For tomography, data were collected at a nominal magnification of ×53,000, corresponding to a calibrated pixel size of 1.276 Å on the specimen level in super-resolution mode. Tilt series between −60° and +60° with a tilt increment of 3° were acquired at selected positions using a grouped dose–symmetric tilt scheme in SerialEM[35]. A video of eight to ten frames was recorded at each tilt angle and the cumulative dosage on the specimen for a tilt series was about 120 electrons per Å^2.

Single-particle cryo-EM reconstruction. The workflow of single-particle analysis is summarized in Extended Data Fig. 1. After data collection, each video was motion corrected and binned 2× to a pixel size of 1.36 Å by MotionCor2 (ref. [36]), yielding two micrographs: a dose-unweighted micrograph (used for manually screening, particle picking and defocus determination) and a dose-weighted micrograph (for particles extraction and final reconstructions). A total of 3,609 good images were selected from 3,961 through manual screening. Then defocus values of micrographs were determined by CTFFIND4 (ref. [37]). Virus particles were picked by ETHAN[38] and then manually checked to add the particles near the edges of image. A total number of 27,138 virus particles were extracted with a box size of 768 pixels and further binned to 384 pixels (2.72 Å per pixel) to speed up data processing in RELION[39,40]. In the first step of our workflow, the overall structure of BTV at low pH was reconstructed by icosahedral symmetry as done for previous reconstructions at high pH 8.8 (ref. [14]). After 2D and 3D classifications, 15,224 good particles were selected and subjected to a 3D autorefinement with icosahedral symmetry yielding a reconstruction with a resolution of 5.44 Å. With the more accurate centre and orientation parameters, the 15,224 viral particles were re-extracted with a box size of 768 pixels (1.36 Å per pixel). These viral particle images and their corresponding icosahedral-related data STAR files were used in the next step.

Due to the unsynchronized nature of conformational changes of different VP5 trimers even on the same BTV particle, we used an icosahedral-reconstruction-guided subparticle reconstruction workflow to obtain near-atomic resolution structures. For the icosahedral reconstruction, there were two VP5 trimers (VP5 trimer 1 and VP5 trimer 2) in each asymmetry unit. In the second step of our workflow, we used a subparticle reconstruction method[30,41,42] centring on the first of the two VP5 trimers. The STAR file of icosahedral reconstruction in step 1 with 15,224 virus particles was expanded by I3 symmetry—60 entries with different orientation for one virus particles. Subparticles were then extracted with a box size of 300 pixels from those viral particle images and subjected to local refinement in RELION, yielding a reconstruction with resolution of 3.2 Å. The VP2 density is visible at a lower threshold, indicating non-uniform occupancy of VP2 across different virions and/or even on the same virion (Extended Data Fig. 1).

In the third step of our workflow, we carried out a focused 3D classification without orientation search using a cylinder mask centred on VP5 trimer 1 by

asking for five classes in RELION[39,40]. The first class which was a mixture of two different states was further classified into two classes. Finally, four different states were obtained with 66,934 particles in IMS1, 103,469 particles in IMS2, 120,974 particles in IMS3 and 572,331 particles in low-pH state. These particles were further subjected to 3D autorefinement, yielding four different conformations: IMS1 at 3.9 Å, IMS2 at 3.8 Å, IMS3 at 3.6 Å and low-pH state at 3.4 Å, respectively.

In the final step, to improve the density quality on the VP5 stalk region in the low-PH state, we used a method by combing the signal subtraction and focused 3D classification in RELION[39,40]. The projection of the low-pH state conformation outside of a soft mask located on VP5 region was subtracted from low-pH state raw subparticles. A total of 75,625 subtracted particles with good stalk density were selected after several rounds of focused 3D classification without orientation search. Then the corresponding original subparticles were subjected to 3D autorefinement yielding a final reconstruction at 4.0 Å. This reconstruction was used to facilitate model building of VP5 stalk in low-pH state. However, most of the distal part was unresolved in the subparticle reconstruction and even with further focused 3D classification, indicating the flexibility of distal portion of the stalk.

The resolution of the cryo-EM map was estimated on the basis of the gold-standard Fourier shell correlation criterion, FSC = 0.143 (ref. [43]). The cryo-EM maps were auto-sharpened by the relion_postprocess programme in RELION[40]. The local resolution evaluations were determined by ResMap[44].

Cryo-ET reconstruction and subtomogram averaging. Tomogram reconstruction and subtomogram averaging were completed similarly as reported before[45]. Briefly, frames in each video were aligned and motion corrected and images were binned to pixel size of 2.55 Å by MotionCor2 (ref. [36]). Defocus value of aligned image in each tilt angle was estimated by CTFFIND4 (ref. [37]). Tilt series were reconstructed with IMOD 4.9 software package[46] by selected gold beads. Estimated defocus value of each image was used as input for ctfphaseflip. Two tomograms were generated by weighted back projection and simultaneous interactive reconstruction technique (SIRT) method, respectively. High-contrast SIRT tomograms were binned 4× (10.2 Å per pixel) by binvol programmme of IMOD[46] for particle picking and display. For low-pH condition, a total number of 33 tomograms with good alignment and contrast were selected and further binned 2× (5.1 Å per pixel) and 4× (10.2 Å per pixel) for further processing.

For subtomogram averaging, particles of the stalk region were manually picked in IMOD[46] and each particle was represented by two points in a contour, with the first one for the capsid-proximal and the second one for the capsid-distal end of the stalk protruding from the virus capsid. Total numbers of 107 and 100 particles were picked for membrane-free stalk and membrane-wrapped stalk, respectively. Subvolume averaging was performed in PEET software[47,48] and 4× binned tomograms were used first. Initial orientations of particles were generated from the manually picked particles by using stalkInit. Angular search was performed with a cylinder mask and average without search was used as initial model. Then the resulting particles were symmetry expanded to C3 along particle Y axis by using ModifyMotiveList programme in IMOD[46]. The angular search was performed with a finer range until it converged. The refinement was then upgraded to 2× binned tomograms with model files and corresponding motive list files resampled from 4× binning to 2× binning. Resolutions of membrane-free stalk and membrane-wrapped stalk were calculated by calcFSC in PEET[47] to 24 and 27 Å, respectively, on the basis of the 0.143 FSC criterion.

Atomic modelling, model refinement and graphics visualization. For the low-pH state, the anchoring domain structure of VP5 at pH 8.8 (PDB 3J9E)[14] was fitted into the low-pH state map (3.4 Å). The model was subsequently manually adjusted in Coot[49]. The stalk of VP5 was built according to the low-pH focus map (4 Å) with guidance from the structure of pH 8.8. Crystal structure of VP7 trimer was fitted into the cryo-EM map in Chimera[50] and locally adjusted in Coot[49]. The model was then refined in real space according to the low-pH state map (3.4 Å) by PHENIX[51] and validated by wwPDB validation server. For the model of VP5 in IMS2, refined atomic model of low-pH state was docked into the cryo-EM map first. The helices of unfurling domain in VP5-B were built in Coot[49] with guidance from the structure of pH 8.8. Visualization of the atomic model, including figures and videos, were accomplished in UCSF Chimera and Chimera X[50].

For the hypothetic model of full-length VP5, atomic structure of VP5 at low pH was fitted into the map of membrane-wrapped stalk from subtomogram averaging. Extension of the stalk with alanine was finished by using the atomic model of postfusion state of SARS-CoV-2 spike (PDB 6M3W)[52] as a template. Then the model was manually adjusted in Coot[49] according to both the membrane-free and membrane-wrapped map of stalk. VP5 structure at high pH was used as a guidance to optimize the fit of model to the map and to minimize the clash within the model.

Structure-guided, site-directed mutagenesis and virus recovery assay. Site-directed mutagenesis was performed to introduce mutations into the exact copy of BTV-1 S5(VP5) or S7 (VP7) (pUC19BTV1T7S5 or pUC19BTV1T7S7) complementary DNA plasmid for virus recovery assay, as previously described[14,20,29]. Briefly, BTV RNA transcripts were generated from the digested cDNA plasmid clones using a mMACHINE T7 transcription kit (Thermo Fisher). A monolayer of BSR cell (BHK-21 subclone) in six-well plates at 100% confluence was transfected with a mixture of ten different BTV RNA transcripts using Lipofectamine 2000 reagent. At 4 h posttransfection, the medium was replaced with a 6-ml overlay consisting of minimal essential medium, 2% FBS and 1.5% (w/v) agarose. Then the plates were incubated at 35 °C in 5% CO_2 for 72 h to allow plaques to appear.

Immunofluorescence. BSR monolayer transfected with 1 μg of wild-type or mutant BTV-1 S6 or S7 RNA segment using EndoFectin according to manufacturer's instruction (GeneCopoeia) was fixed in 4% paraformaldehyde and then permeablized with 0.1% Triton X-100 in phosphate-buffered saline. The guinea pig anti-VP5 or anti-VP7 antibody at 1:1,000 dilution was used to detect VP5 or VP7, using the relevant secondary fluorescent antibody (Goat anti-Guinea Pig IgG (H + L), Alexa Fluor 488, Thermo Fisher A-11073) at 1:2,000 dilution. Nuclei were stained with Hoechst. Images were captured using the LSM880 inverted confocal microscope (Carl Zeiss).

Pull-down analysis. WT or Q418A mutant VP5 with strep tag were co-expressed with WT VP7 in insect cells for 48 h. Strep-Tactin beads were added to the cell lysate to allow binding of VP5 at pH 8.0. After SDS–PAGE, VP7 interacting with VP5 was detected by western blot using a guinea pig anti-VP7 as primary antibody and the related secondary antibody (Goat anti-Guinea Pig IgG Alkaline phosphate, Sigma, SAB3700352) at 1:5,000 dilution.

Liposome calcein release assay. A total 5 μg of the lipid with a ratio of 50:20:3:4:8:15 PC/PE/SM/PS/PI/LBPA (Sigma) in 1 ml of the calcein buffer (50 mM calcein, 100 mM NaCl, 10 mM Na_2PO_4 and 2 mM KH_2PO_4) was prepared using a mini extruder with a 0.1 μM polycarbonate membrane (Avanti Polar Lipids). Unencapsulated calcein was removed by size exclusion chromatography. Wild-type or mutant VP5 protein were purified the same way as describe before[14] and validated by gel-filtration chromatography in a Superdex 200 Increase 10/300 GL column in the buffer containing 10 mM Tris-HCl at pH 8.0, 150 mM NaCl and 5% (w/v) glycerol. The wild-type protein was further verified by negative stain with 2% tungsten phosphate 7.5 for the high-pH condition and sodium citrate 5.5 and 2% uranyl acetate for the low-pH condition. Proteins were mixed with calcein-loaded liposomes at a final concentration of 0.1 mg ml^{-1} and incubated at room temperature for 10 min. The mixture was then acidified to pH 5.5 with 1 N HCl and incubated for 20 min at 37 °C. Fluorescence was measured and then the percentage of calcein release was calculated as previously described[14].

Statistics and reproducibility. No statistical method was used to predetermine sample size. No data were excluded from the analyses. Functional assays including virus recovery assay and pull-down assay were independently repeated twice; representative results are shown in Figs. 3f and 4i and Extended Data Fig. 7a–d. Results shown in Fig. 4j are from two independent experiments. All of the experiments of pH-induced conformational change of BTV and VP5 (Fig. 4a-h and Extended Data Figs. 2a–c, 7e-f and 8) were repeated independently for two times with similar results. In general, each experiment shown in this paper was repeated independently at least twice with similar outcomes.

Reporting Summary. Further information on research design is available in the Nature Research Reporting Summary linked to this article.

Data availability

The cryo-EM density maps were deposited in the Electron Microscopy Data Bank (EMDB) with accession codes IMS1 (EMD-24686), IMS2 (EMD-24685), IMS3 (EMD-24687) and low-pH state (EMD-24684). The corresponding models of VP5 were deposited in the Protein Data Bank (PDB) with IMS2 (7RTO) and low-pH state (7RTN). Source data are provided with this paper. All other data are available from the authors on reasonable request.

Received: 22 January 2021; Accepted: 22 September 2021;
Published online: 26 October 2021

References

1. Benton, D. J., Gamblin, S. J., Rosenthal, P. B. & Skehel, J. J. Structural transitions in influenza haemagglutinin at membrane fusion pH. *Nature* **583**, 150–153 (2020).
2. Chen, B. Molecular mechanism of HIV-1 entry. *Trends Microbiol.* **27**, 878–891 (2019).
3. Cai, Y. et al. Distinct conformational states of SARS-CoV-2 spike protein. *Science* **369**, 1586–1592 (2020).
4. Mercer, J., Lee, J. E., Saphire, E. O. & Freeman, S. A. SnapShot: enveloped virus entry. *Cell* **182**, 786–786 (2020).
5. Harrison, S. C. Viral membrane fusion. *Nat. Struct. Mol. Biol.* **15**, 690–698 (2008).
6. Kielian, M. Mechanisms of virus membrane fusion proteins. *Annu Rev. Virol.* **1**, 171–189 (2014).

7. Tsai, B. Penetration of nonenveloped viruses into the cytoplasm. *Annu. Rev. Cell Dev. Biol.* **23**, 23–43 (2007).
8. Kumar, C. S., Dey, D., Ghosh, S. & Banerjee, M. Breach: host membrane penetration and entry by nonenveloped viruses. *Trends Microbiol.* **26**, 525–537 (2018).
9. Roy, P. Bluetongue virus genetics and genome structure. *Virus Res.* **13**, 179–206 (1989).
10. Patel, A. & Roy, P. The molecular biology of bluetongue virus replication. *Virus Res.* **182**, 5–20 (2014).
11. Grimes, J. M. et al. The atomic structure of the bluetongue virus core. *Nature* **395**, 470–478 (1998).
12. Roy, P. Bluetongue virus structure and assembly. *Curr. Opin. Virol.* **24**, 115–123 (2017).
13. Zhang, X. et al. Bluetongue virus coat protein VP2 contains sialic acid-binding domains, and VP5 resembles enveloped virus fusion proteins. *Proc. Natl Acad. Sci. USA* **107**, 6292–6297 (2010).
14. Zhang, X. et al. Atomic model of a nonenveloped virus reveals pH sensors for a coordinated process of cell entry. *Nat. Struct. Mol. Biol.* **23**, 74–80 (2016).
15. Liemann, S., Chandran, K., Baker, T. S., Nibert, M. L. & Harrison, S. C. Structure of the reovirus membrane-penetration protein, Mu1, in a complex with is protector protein, Sigma3. *Cell* **108**, 283–295 (2002).
16. Dormitzer, P. R., Nason, E. B., Prasad, B. V. & Harrison, S. C. Structural rearrangements in the membrane penetration protein of a non-enveloped virus. *Nature* **430**, 1053–1058 (2004).
17. Swanson, K. et al. Structure of the Newcastle disease virus F protein in the post-fusion conformation. *Virology* **402**, 372–379 (2010).
18. Das, D. K. et al. Direct visualization of the conformational dynamics of single influenza hemagglutinin trimers. *Cell* **174**, 926–937 (2018).
19. Boyce, M. & Roy, P. Recovery of infectious bluetongue virus from RNA. *J. Virol.* **81**, 2179–2186 (2007).
20. Boyce, M., Celma, C. C. & Roy, P. Development of reverse genetics systems for bluetongue virus: recovery of infectious virus from synthetic RNA transcripts. *J. Virol.* **82**, 8339–8348 (2008).
21. Agosto, M. A., Ivanovic, T. & Nibert, M. L. Mammalian reovirus, a nonfusogenic nonenveloped virus, forms size-selective pores in a model membrane. *Proc. Natl Acad. Sci. USA* **103**, 16496–16501 (2006).
22. Heo, W. D. et al. PI(3,4,5)P-3 and PI(4,5)P-2 lipids target proteins with polybasic clusters to the plasma membrane. *Science* **314**, 1458–1461 (2006).
23. Stahelin, R. V. Lipid binding domains: more than simple lipid effectors. *J. Lipid Res.* **50**, S299–S304 (2009).
24. Kobayashi, T. et al. Late endosomal membranes rich in lysobisphosphatidic acid regulate cholesterol transport. *Nat. Cell Biol.* **1**, 113–118 (1999).
25. Bissig, C. & Gruenberg, J. Lipid sorting and multivesicular endosome biogenesis. *Cold Spring Harb. Perspect. Biol.* **5**, a016816 (2013).
26. Patel, A., Mohl, B. P. & Roy, P. Entry of bluetongue virus capsid requires the late endosome-specific lipid lysobisphosphatidic acid. *J. Biol. Chem.* **291**, 12408–12419 (2016).
27. Bhattacharya, B. & Roy, P. Bluetongue virus outer capsid protein VP5 interacts with membrane lipid rafts via a SNARE domain. *J. Virol.* **82**, 10600–10612 (2008).
28. Hassan, S. H., Wirblich, C., Forzan, M. & Roy, P. Expression and functional characterization of bluetongue virus VP5 protein: role in cellular permeabilization. *J. Virol.* **75**, 8356–8367 (2001).
29. Forzan, M., Marsh, M. & Roy, P. Bluetongue virus entry into cells. *J. Virol.* **81**, 4819–4827 (2007).
30. He, Y. et al. In situ structures of RNA-dependent RNA polymerase inside bluetongue virus before and after uncoating. *Proc. Natl Acad. Sci. USA* **116**, 16535–16540 (2019).
31. Cui, Y., Zhang, Y., Zhou, K., Sun, J. & Zhou, Z. H. Conservative transcription in three steps visualized in a double-stranded RNA virus. *Nat. Struct. Mol. Biol.* **26**, 1023–1034 (2019).
32. Herrmann, T. et al. Functional refolding of the penetration protein on a non-enveloped virus. *Nature* **590**, 666–670 (2021).
33. Mertens, P. P., Burroughs, J. N. & Anderson, J. Purification and properties of virus particles, infectious subviral particles, and cores of bluetongue virus serotypes 1 and 4. *Virology* **157**, 375–386 (1987).
34. Halldorsson, S. et al. Shielding and activation of a viral membrane fusion protein. *Nat. Commun.* **9**, 349 (2018).
35. Mastronarde, D. N. Automated electron microscope tomography using robust prediction of specimen movements. *J. Struct. Biol.* **152**, 36–51 (2005).
36. Zheng, S. Q. et al. MotionCor2: anisotropic correction of beam-induced motion for improved cryo-electron microscopy. *Nat. Methods* **14**, 331–332 (2017).
37. Rohou, A. & Grigorieff, N. CTFFIND4: fast and accurate defocus estimation from electron micrographs. *J. Struct. Biol.* **192**, 216–221 (2015).
38. Kivioja, T., Ravantti, J., Verkhovsky, A., Ukkonen, E. & Bamford, D. Local average intensity-based method for identifying spherical particles in electron micrographs. *J. Struct. Biol.* **131**, 126–134 (2000).
39. Scheres, S. H. Processing of structurally heterogeneous cryo-EM data in RELION. *Methods Enzymol.* **579**, 125–157 (2016).
40. Scheres, S. H. RELION: implementation of a Bayesian approach to cryo-EM structure determination. *J. Struct. Biol.* **180**, 519–530 (2012).
41. Ilca, S. L. et al. Localized reconstruction of subunits from electron cryomicroscopy images of macromolecular complexes. *Nat. Commun.* **6**, 8843 (2015).
42. Liu, Y. T., Jih, J., Dai, X., Bi, G. Q. & Zhou, Z. H. Cryo-EM structures of herpes simplex virus type 1 portal vertex and packaged genome. *Nature* **570**, 257–261 (2019).
43. Rosenthal, P. B. & Henderson, R. Optimal determination of particle orientation, absolute hand, and contrast loss in single-particle electron cryomicroscopy. *J. Mol. Biol.* **333**, 721–745 (2003).
44. Kucukelbir, A., Sigworth, F. J. & Tagare, H. D. Quantifying the local resolution of cryo-EM density maps. *Nat. Methods* **11**, 63–65 (2014).
45. Si, Z. et al. Different functional states of fusion protein gB revealed on human cytomegalovirus by cryo electron tomography with Volta phase plate. *PLoS Pathog.* **14**, e1007452 (2018).
46. Kremer, J. R., Mastronarde, D. N. & McIntosh, J. R. Computer visualization of three-dimensional image data using IMOD. *J. Struct. Biol.* **116**, 71–76 (1996).
47. Nicastro, D. et al. The molecular architecture of axonemes revealed by cryoelectron tomography. *Science* **313**, 944–948 (2006).
48. Heumann, J. M., Hoenger, A. & Mastronarde, D. N. Clustering and variance maps for cryo-electron tomography using wedge-masked differences. *J. Struct. Biol.* **175**, 288–299 (2011).
49. Emsley, P. & Cowtan, K. Coot: model-building tools for molecular graphics. *Acta Crystallogr. D* **60**, 2126–2132 (2004).
50. Pettersen, E. F. et al. UCSF Chimera—a visualization system for exploratory research and analysis. *J. Comput. Chem.* **25**, 1605–1612 (2004).
51. Adams, P. D. et al. PHENIX: a comprehensive Python-based system for macromolecular structure solution. *Acta Crystallogr D* **66**, 213–221 (2010).
52. Fan, X., Cao, D., Kong, L. & Zhang, X. Cryo-EM analysis of the post-fusion structure of the SARS-CoV spike glycoprotein. *Nat. Commun.* **11**, 3618 (2020).

Acknowledgements

We thank T. Nguyen for proof-reading the manuscript. This project is supported in part by grants from the US National Instutitutes of Health (NIH) (AI094386 to Z.H.Z.) and the Wellcome Trust, UK (WT100218; Investigator Award to P.R.). We acknowledge the use of instruments at the Electron Imaging Center for Nanomachines supported by the University of California, Los Angeles, and grants from the NIH (1S10OD018111 and 1U24GM116792) and the National Science Foundation (DBI-1338135 and DMR-1548924).

Author contributions

Z.H.Z. conceived the project. X.X. prepared samples, recorded negative stain EM and cryo-EM images, and processed the data. Y.C. helped with cryo-EM imaging and data processing. W.W. and P.R. performed structure-based mutagenesis and virus recovery analysis, generated recombinant proteins and performed liposome assay and confocal microscopy. X.X. and Z.H.Z. interpreted results and wrote the paper. All authors edited and approved the paper.

Competing interests

The authors declare no competing interests.

Additional information

Extended data is available for this paper at https://doi.org/10.1038/s41564-021-00988-8.

Supplementary information The online version contains supplementary material available at https://doi.org/10.1038/s41564-021-00988-8.

Correspondence and requests for materials should be addressed to Z. Hong Zhou.

Peer review information *Nature Microbiology* thanks Juha Huiskonen and the other, anonymous, reviewer(s) for their contribution to the peer review of this work. Peer reviewer reports are available.

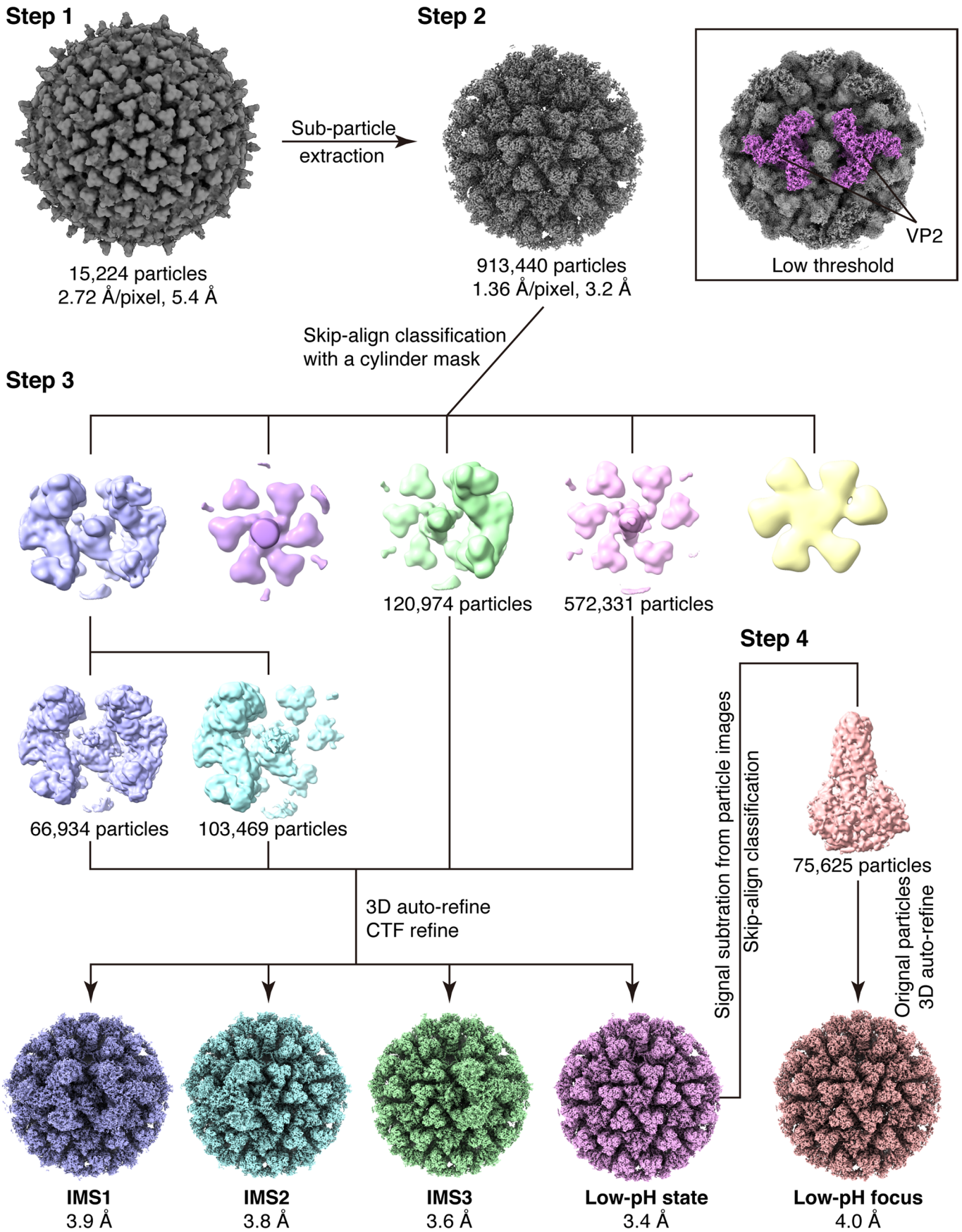

Extended Data Fig. 1 | See next page for caption.

Extended Data Fig. 1 | Data processing workflow for subparticle reconstruction. After icosahedral reconstruction (step 1) of BTV, subparticles centred on VP5 trimer 1 were extracted from images of virus particles and subjected to refinement (step 2). The same map obtained in this step is shown in the box at a lower threshold so that VP2 trimers are visible. Classification of the subparticle reconstruction resulted in four different structures, as judged from the presence/absence of VP2 (step 3). Further classification focused on VP5 resulted in a map with improved density for the VP5 stalk (step 4).

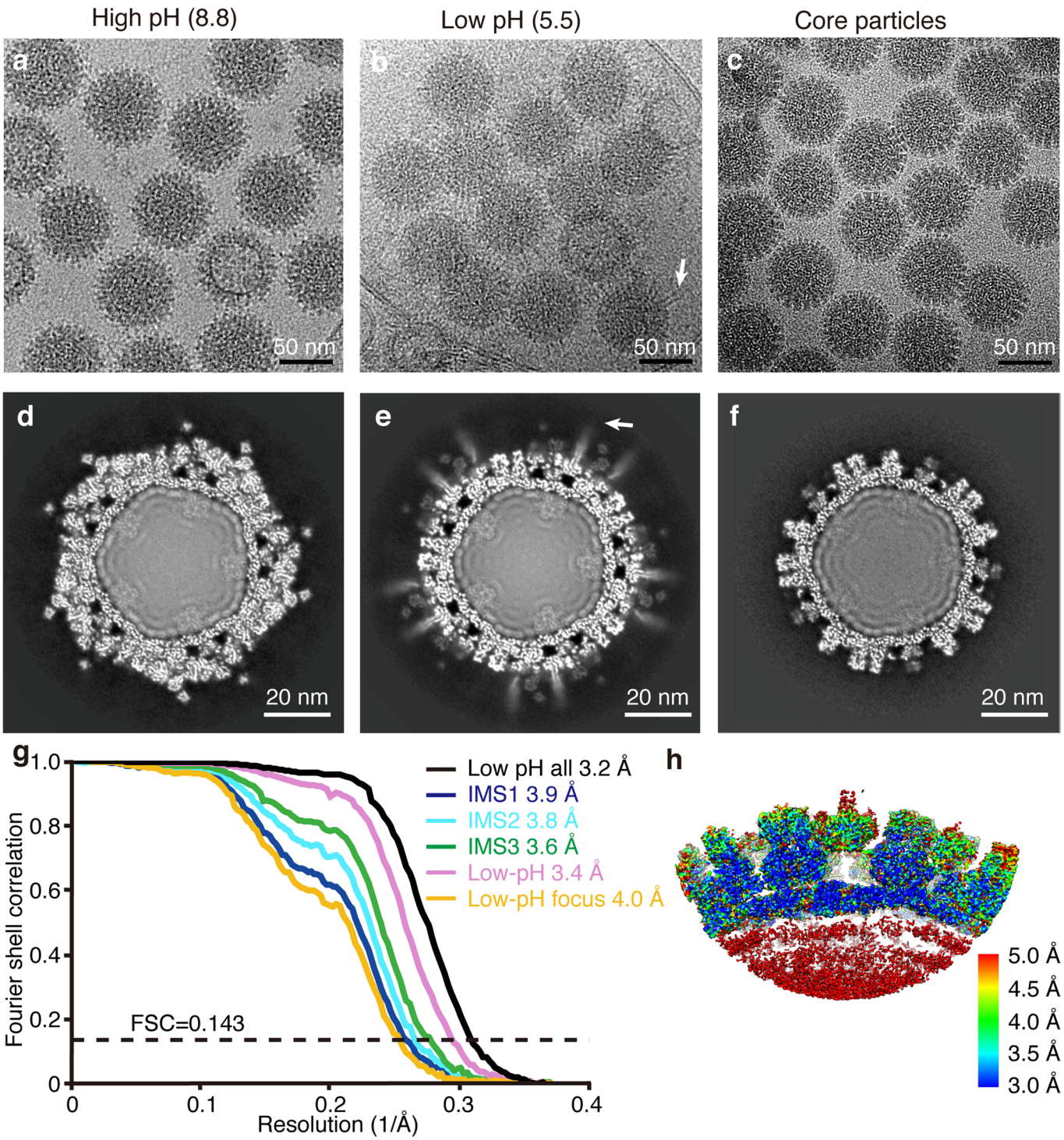

Extended Data Fig. 2 | Cryo-EM image acquisition, 3D reconstructions and resolution assessment. a-c, Representative cryo-EM images from two independent experiments for BTV at high pH (**a**), BTV at low pH (**b**) and BTV cores (**c**). **d-f**, Slices from the icosahedral reconstructions (low-pass-filtered to 6 Å) of BTV at high pH (**d**), BTV at low pH (**e**) and BTV core (**f**). Arrows in (**b**) and (**e**) indicate VP5 stalks. **g**, Gold-standard Fourier shell correlation (FSC) coefficients as a function of spatial frequency for the subparticle reconstructions of BTV in different states. **h**, ResMap[44] local resolution heat map of the subparticle reconstructions of BTV in low-pH state.

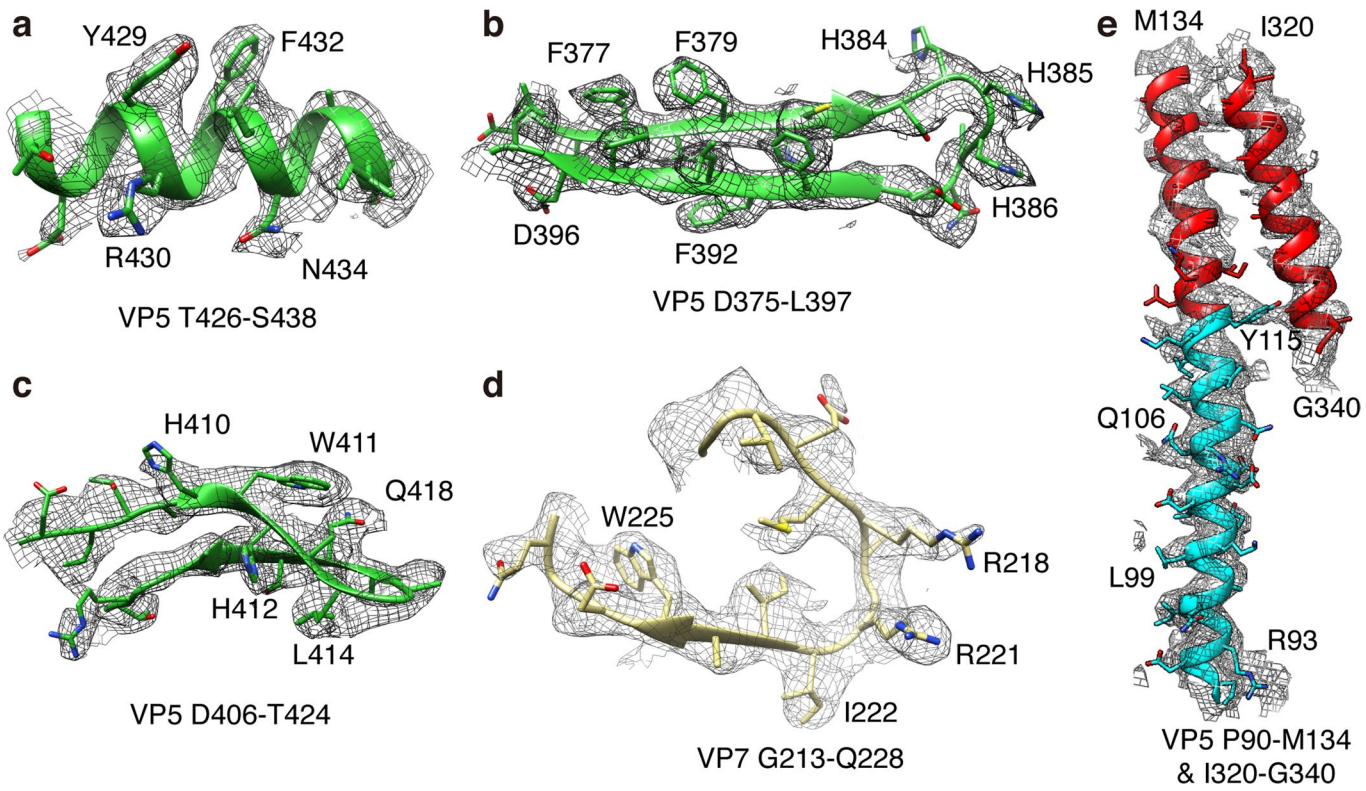

Extended Data Fig. 3 | Superimposition of cryo-EM densities with the atomic model for representative regions of VP5 and VP7 in low-pH state. **a**,**b**, Representative density map of α helices (**a**) and β strands (**b**). **c**, Density map of the anchoring β-hairpin in one subunit of the VP5 trimer. **d**, Density map of the region in VP7 which interacts with the anchoring β-hairpin of VP5. **e**, Density map of the region in VP5 6-helix stalk in one subunit.

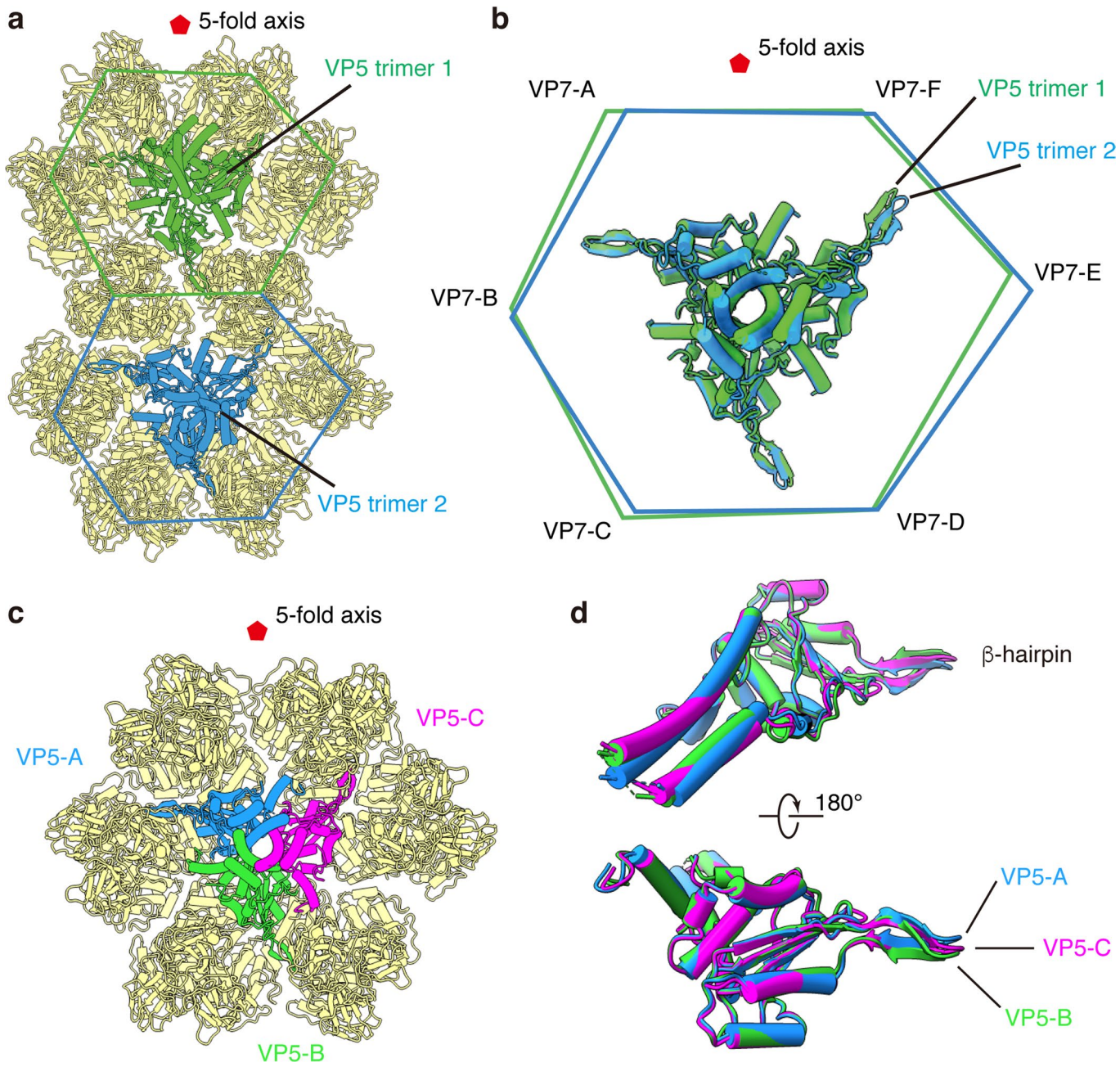

Extended Data Fig. 4 | Comparison of structures of VP5 subunits within an asymmetric unit. a,**b**, Comparison of the two VP5 trimers in an asymmetric unit of BTV in low-pH state. The VP5 trimer is represented by cylinders (for α helices) and ribbons (for β sheets), whereas the six surrounding VP7 trimers by a hexagon (each vertex of the hexagon is the centre of the three G199 residues in each VP7 trimer). The two vp5 trimers are superposed in (**b**). **c**,**d**, Comparison of the three subunits of VP5 trimer 1. Three subunits in VP5 trimer 1 are named VP5-A VP5-B and VP5-C in anticlockwise direction from 5-fold axis. VP5-A, VP5-B and VP5-C are superposed in (**d**).

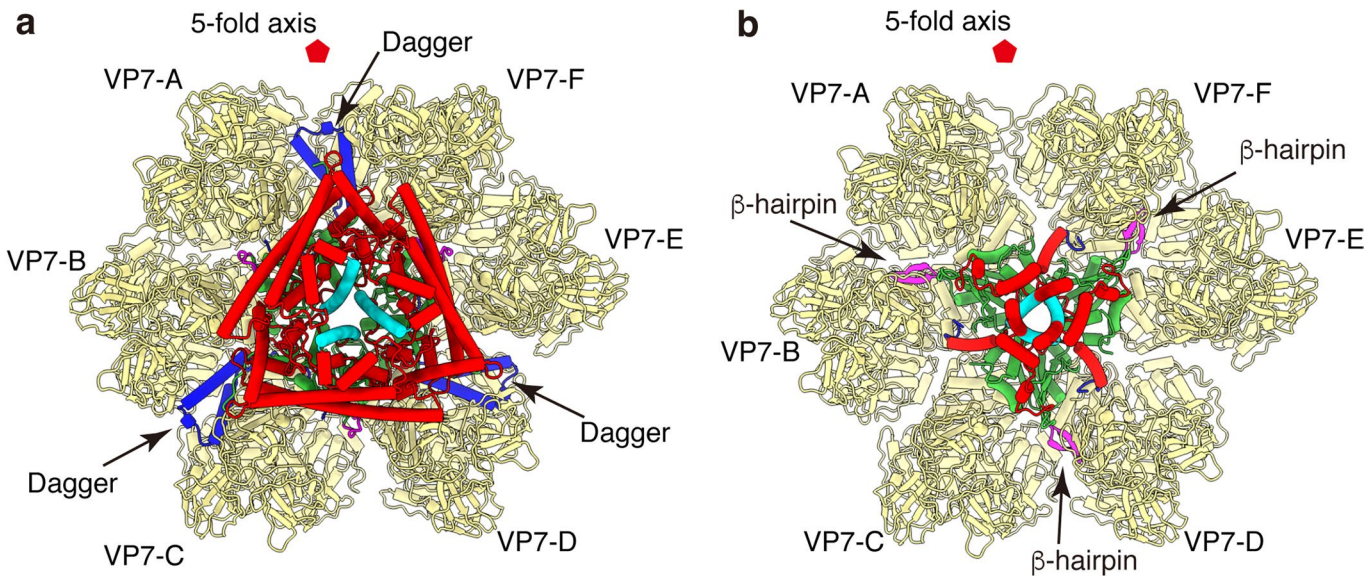

Extended Data Fig. 5 | Anchorage of VP5 in different pH conditions. a, Anchorage of the VP5 trimer to the surrounding VP7 at pH 8.8 by the dagger domains. The dagger domain inserts into the interface between VP7-A and F, or VP7-B and C or VP7-D and E. **b**, Anchorage of the VP5 trimer to the surrounding VP7 at pH 5.5 by the anchoring β-hairpins. The β-hairpin inserts into the interface between VP7-A and B, or VP7-C and D or VP7-E and F. VP5 is coloured the same as in Fig. 2b except that the β-hairpins are in magenta.

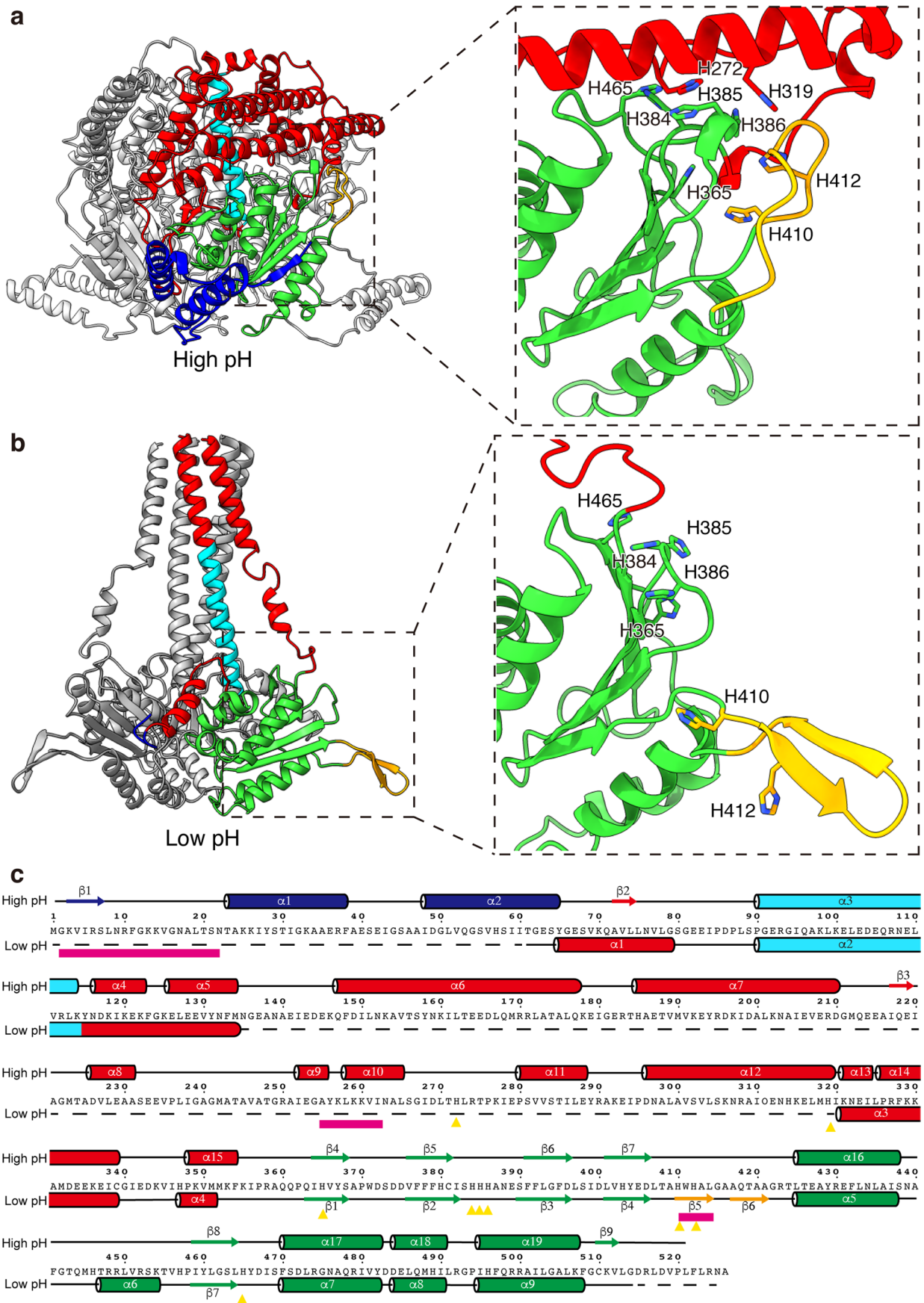

Extended Data Fig. 6 | See next page for caption.

Extended Data Fig. 6 | Structural comparison of VP5 in different pH conditions. a, Interactions of the VP5 pH sensor at pH 8.8 with side chains of important histidine residues shown in stick. **b**, Locations of the important histidine residues at pH 5.5. **c**, Alignment of the second structures of VP5 at high pH and low pH. Portions of VP5 that cannot be traced are indicated by dashed lines. Residues involved the the pH sensor of VP5 are indicated by yellow triangles. Magenta bars show the regions of three membrane penetration elements.

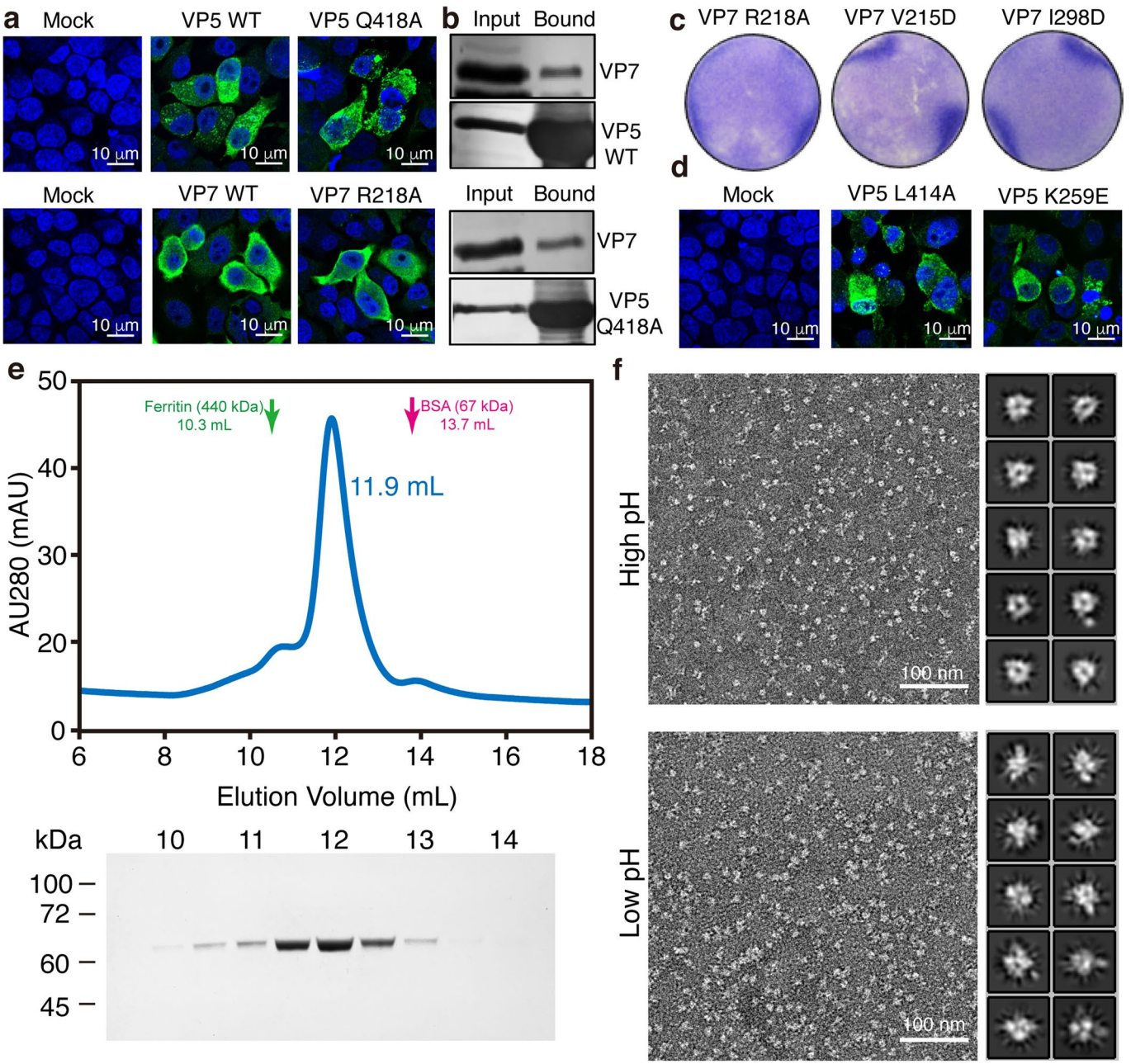

Extended Data Fig. 7 | Virus recovery assay and validation of the purified VP5. a, Representative images of two independent experiments from confocal microscopy. Results confirmed that the expressions of mutant proteins were similar to that of the wild type. **b**, Representative images from two independent experiments for pull-down analysis showing the interactions between VP5 (WT or Q418A) and VP7 at high pH. **c**, Plaque formation at 72 hours post-transfection by reverse genetics with BTV genome carrying VP7 mutations in the interaction interface with β-hairpin. **d**, Representative images of two independent experiments from confocal microscopy for mutants in the membrane penetration elements. **e**, Gel-filtration chromatography and SDS-gel of the purified VP5. Arrows indicate the elution volumes of the markers (Ferritin and BSA). Results represent for two independent purification experiments. **f**, Negative stain analysis of the purified VP5 in high-pH and low-pH conditions. Images of 2D class averages are shown on the right of the panels. The data shown are representative results of two independent experiments.

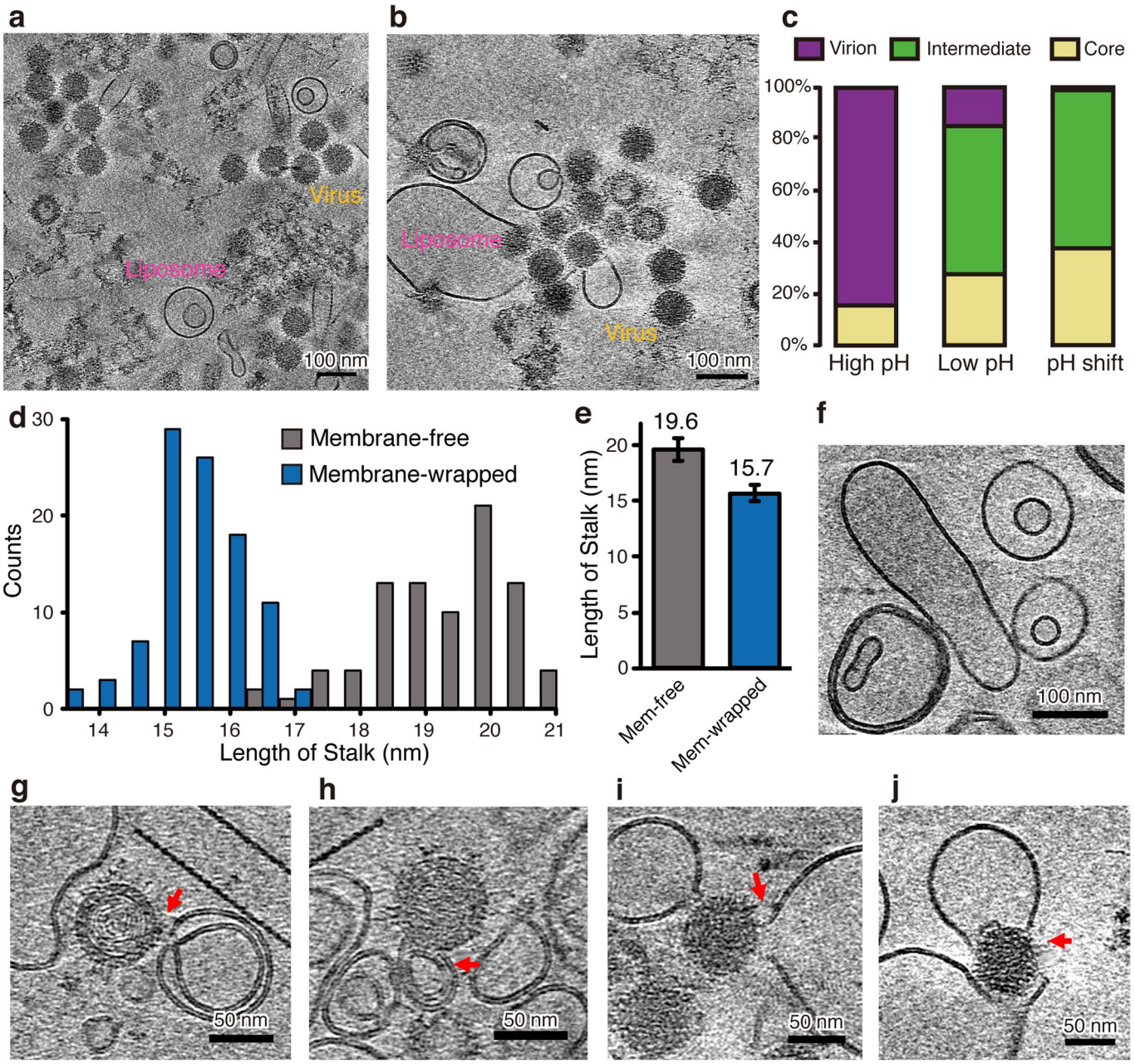

Extended Data Fig. 8 | BTV interacts with membrane. a, A slice from a representative cryo-ET reconstruction of BTV with liposomes at neutral pH. The virus and the liposome are labelled. No interactions between the virus and the liposome were observed in the tomograms collected. **b**, A slice from a representative cryo-ET reconstruction of BTV with liposomes in pH-shift condition. **c**, Proportion of BTV virion, intermediate and core in three different pH conditions. Numbers of particles counted for high pH, low pH and pH-shift condition are 317, 510 and 360, respectively. **d**,**e**, Length of the membrane-free and membrane-wrapped VP5 stalks in low-pH condition. The length of stalk which shown clearly density in the low-pH tomograms was measured in IMOD[46]. The measurements within every 0.5 nm were counted and plotted as histogram in (**d**) for membrane-free stalks (n = 85 biologically independent measurements) and membrane-wrapped stalks (n = 98 biologically independent measurements), respectively. Averaged lengths (mean ± s.d.) are shown in (**e**). **f**, A slice of a representative tomogram of free liposome sample. **g-i**, Typical examples of BTV in the act of membrane penetration. (**g**) and (**h**) are from tomograms of low-pH condition while (**i**) and (**j**) are from tomograms of pH-shift condition. Red arrows indicate the membrane pores generated by BTV. For (**a-j**), experiments were repeated independently for two times and representative results are shown here.

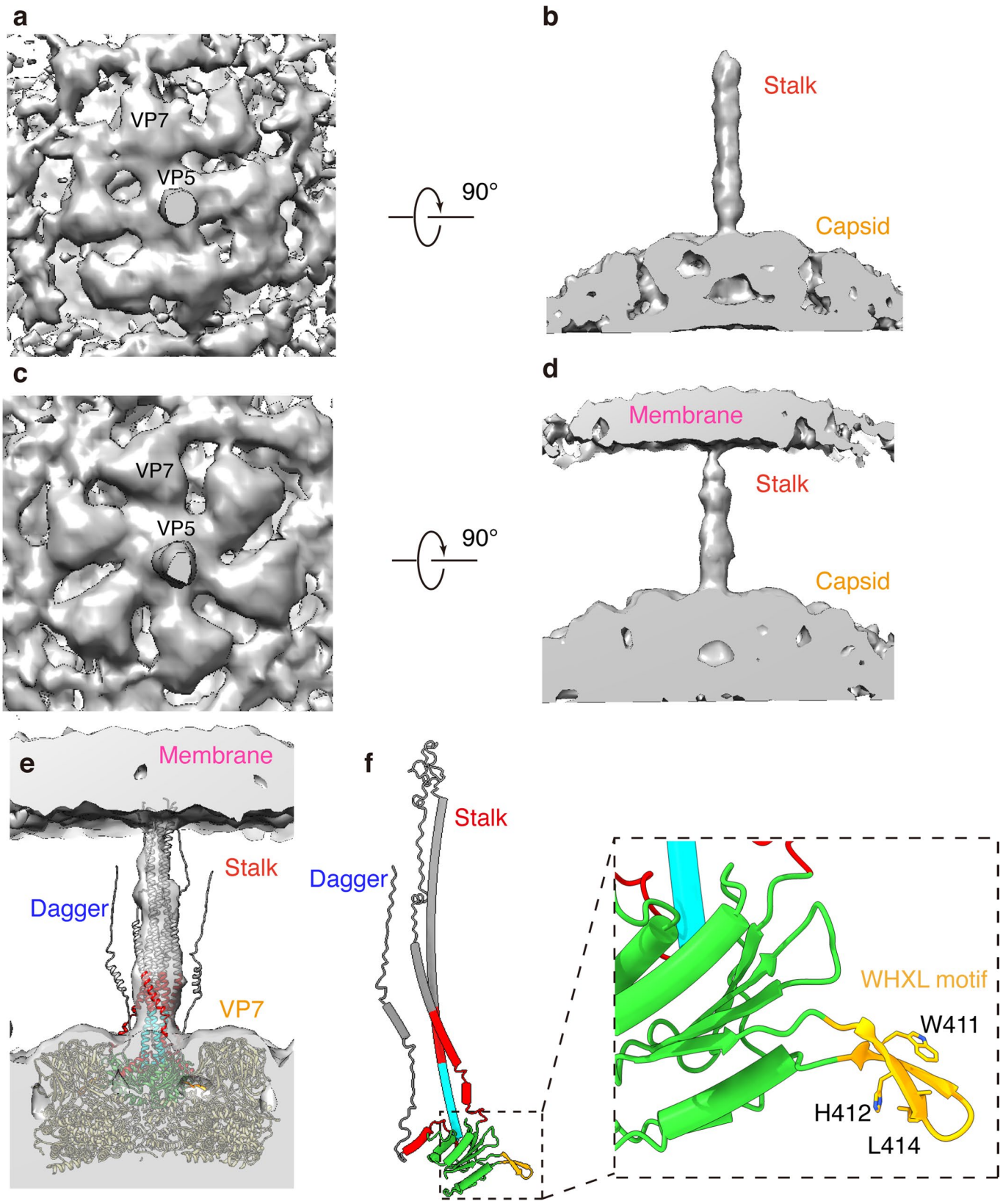

Extended Data Fig. 9 | Subtomogram averages of the VP5 stalk. a-b, Top (**a**) and side (**b**) surface views of the subtomogram average of the membrane-free stalk. **c-d**, Top (**c**) and side (**d**) surface views of the subtomogram average of the membrane-wrapped stalk. **e**, Superimposition of the hypothetic model of full-length VP5 trimer and surface view of the subtomogram average map of the membrane-wrapped stalk from (**d**) at a lower threshold. **f**, Side view of one subunit of the full-length model of VP5 trimer highlighting the three important elements (the dagger domain, the WHAL motif and the stalk) for membrane penetration. The hypothetic models for the untraceable parts (dagger and stalk tip) are coloured in grey.

nature research

Corresponding author(s): Z. Hong Zhou

Last updated by author(s): 03_9-2021

Reporting Summary

Nature Research wishes to improve the reproducibility of the work that we publish. This form provides structure for consistency and transparency in reporting. For further information on Nature Research policies, see our Editorial Policies and the Editorial Policy Checklist.

Statistics

For all statistical analyses, confirm that the following items are present in the figure legend, table legend, main text, or Methods section.

n/a	Confirmed	
☐	☒	The exact sample size (*n*) for each experimental group/condition, given as a discrete number and unit of measurement
☐	☒	A statement on whether measurements were taken from distinct samples or whether the same sample was measured repeatedly
☒	☐	The statistical test(s) used AND whether they are one- or two-sided *Only common tests should be described solely by name; describe more complex techniques in the Methods section.*
☒	☐	A description of all covariates tested
☒	☐	A description of any assumptions or corrections, such as tests of normality and adjustment for multiple comparisons
☐	☒	A full description of the statistical parameters including central tendency (e.g. means) or other basic estimates (e.g. regression coefficient) AND variation (e.g. standard deviation) or associated estimates of uncertainty (e.g. confidence intervals)
☒	☐	For null hypothesis testing, the test statistic (e.g. *F*, *t*, *r*) with confidence intervals, effect sizes, degrees of freedom and *P* value noted *Give P values as exact values whenever suitable.*
☒	☐	For Bayesian analysis, information on the choice of priors and Markov chain Monte Carlo settings
☒	☐	For hierarchical and complex designs, identification of the appropriate level for tests and full reporting of outcomes
☒	☐	Estimates of effect sizes (e.g. Cohen's *d*, Pearson's *r*), indicating how they were calculated

Our web collection on statistics for biologists contains articles on many of the points above.

Software and code

Policy information about availability of computer code

Data collection	SerialEM 3.8
Data analysis	ETHAN 1.0, CTFFIND4, RELION3.0, IMOD 4.9, PEET(within IMOD 4.9), UCSF Chimera 1.13 and ChimeraX 1.25, Resmap1.95, MotionCor2, Coot0.8.9, PHENIX 1.19

For manuscripts utilizing custom algorithms or software that are central to the research but not yet described in published literature, software must be made available to editors and reviewers. We strongly encourage code deposition in a community repository (e.g. GitHub). See the Nature Research guidelines for submitting code & software for further information.

Data

Policy information about availability of data

All manuscripts must include a data availability statement. This statement should provide the following information, where applicable:

- Accession codes, unique identifiers, or web links for publicly available datasets
- A list of figures that have associated raw data
- A description of any restrictions on data availability

The cryo-EM density maps were deposited in the Electron Microscopy Data Bank (EMDB) with accession code IMS1 (EMD-24686), IMS2 (EMD-24685), IMS3 (EMD-24687), low-pH state (EMD-24684). The corresponding models of VP5 were deposited in the Protein Data Bank (PDB) with IMS2 (7RTO) and low-pH state (7RTN). Uncropped gels (Extended Data Fig. 7b and 7e) and quantification raw data (Fig. 4i and Extended Data Fig. 8c-e) are provided as source data with this paper. All other data are available from the authors on reasonable request.
Previously published atomic models used in this paper (3J9E and 6M3W) are available from Protein Data Bank.
Protein sequence of VP5 is from Uniprot (K7QP12).

Field-specific reporting

Please select the one below that is the best fit for your research. If you are not sure, read the appropriate sections before making your selection.

☒ Life sciences ☐ Behavioural & social sciences ☐ Ecological, evolutionary & environmental sciences

For a reference copy of the document with all sections, see nature.com/documents/nr-reporting-summary-flat.pdf

Life sciences study design

All studies must disclose on these points even when the disclosure is negative.

Sample size	No statistical methods were used to predetermine sample size. 10 T175 flasks of baby hamster kidney cells were used each time for BTV purification, which can provide enough sample for cryo-EM analysis. Cryo-EM 3D reconstructions were calculated from 3961 images (15224 virus particles for icosahedral reconstruction). The data size is comparable to other studies in this field. The number of particles used for each final map is sufficient to obtain reliable classification and reconstruction results by cryo-EM.
Data exclusions	For cryo-EM analysis, particles that do not belong to the class of interest or have poor qualities based on well established cryoEM principle were excluded after rounds of 2D and 3D classification. This is standard practice required to obtain high resolution cryo EM structure of the class of interest. For functional studies, no data were excluded from any analysis.
Replication	Experiments of low-pH-induced structural rearrangement of VP5 or BTV on cryo-EM grids were repeated two or three times independently with similar results. All biochemical experiments were replicated successfully. The related replicative results were used for quantification and statistical analyses, which are provided in the source data and described in the figure legends accordingly.
Randomization	For cryo-EM, datasets were randomly split into two half for refinements and cross correlation coefficients (FSC curves) between two the half sets are provided in the Extended Data Fig. 2g. For the biochemical experiments, randomization is not applicable to our study, because no grouping was needed.
Blinding	For cryo-EM, datasets were automatically split into two half in Relion, blinding is not feasible. For the biochemical experiments, blinding is not applicable as no grouping was needed for this study.

Reporting for specific materials, systems and methods

We require information from authors about some types of materials, experimental systems and methods used in many studies. Here, indicate whether each material, system or method listed is relevant to your study. If you are not sure if a list item applies to your research, read the appropriate section before selecting a response.

Materials & experimental systems

n/a	Involved in the study
☐	☒ Antibodies
☐	☒ Eukaryotic cell lines
☒	☐ Palaeontology and archaeology
☒	☐ Animals and other organisms
☒	☐ Human research participants
☒	☐ Clinical data
☒	☐ Dual use research of concern

Methods

n/a	Involved in the study
☒	☐ ChIP-seq
☒	☐ Flow cytometry
☒	☐ MRI-based neuroimaging

Antibodies

Antibodies used	Guinea pig anti-VP7 and anti-VP5 (home-made in Roy's lab; 1:1000 dilution); Goat anti-Guinea Pig IgG (H+L) Alexa Fluor 488 (Thermofisher A-11073; 1:2000 dilution); Goat anti-Guinea Pig IgG Alkaline phosphate (Sigma, SAB3700352; 1:5000 dilution)
Validation	All antibodies used are well-validated in previous published paper: Patel, A., Mohl, B. P. & Roy, P. Entry of Bluetongue Virus Capsid Requires the Late Endosome-specific Lipid Lysobisphosphatidic Acid. J Biol Chem 291, 12408-12419, doi:10.1074/jbc.M115.700856 (2016).

Eukaryotic cell lines

Policy information about cell lines

Cell line source(s)	Baby hamster kidney-21 cells (BHK-21) and BSR cells (derived from BHK-21) were from ATCC, Insect cells (SF9 cells, purchased from the Invitrogen Company)

Authentication	No authentication was performed
Mycoplasma contamination	Cell line tested negative for Mycoplasma contamination
Commonly misidentified lines (See ICLAC register)	The BHK-21, BSR and SF9 cell lines are not listed in ICLAC as commonly misidentified cell lines. In addition, the cells themselves are not being studied, instead they are used as tools for virus generation or recombinant protein expression.